Supplementary Information for

Systematic design and functionalisation of amorphous zirconium metal-organic frameworks

Nattapol Ma,* Soracha Kosasang, Jennifer Theissen, Nick Gys,
Tom Hauffman, Ken-ichi Otake, Satoshi Horike, and Rob Ameloot*

Correspondence to: ma.nattapol@nims.go.jp and rob.ameloot@kuleuven.be

Methods

Synthesis of $Zr_6O_4(OH)_4(C_2H_3O_2)_8(H_2O)Cl_3$ (ZrOAc)

$ZrCl_4$ (99.5%, metal basis) and acetic acid (glacial) were purchased from Thermo Fisher Scientific. 2-Propanol (>99.8, GC, ACS reagent) was purchased from Merck. All chemicals were used without further purification. The synthesis was adapted from ref. [1]. $ZrCl_4$ powder (31.25 g) was added to a mixture of acetic acid (46.9 mL) and 2-propanol (78.1 mL) under reflux at 100 °C for 60 min. Note that the addition of $ZrCl_4$ to 2-propanol is highly exothermic and should be done with care. The obtained precipitate was filtered and washed with 2-propanol (300 mL), acetone (200 mL), and dried under vacuum at room temperature.

Sol-gel synthesis of amorphous Zr metal-organic frameworks with succinate linker (Zr-*n*L_1)

The ZrOAc (60.0 mg), synthesized in the previous step, was dissolved in Milli-Q water (0.5 mL). The solution was added into an aqueous solution of succinic acid (4, 8, or 12 molar equivalents, 99%, Acros Organics NV) and Milli-Q water (4.5 mL, MilliporeSigma™ Direct-Q™) in a 22-ml glass vial. The vial was then capped and heated in a preheated oven at 80 °C for 72 h to ensure gelation equilibrium was reached. Cross-linking results in gel phases. The gels were then washed with Milli-Q water (20 mL) for 4 cycles, followed by solvent exchange with fresh ethanol (99.8%, Acros Organics NV), then dried at 80 °C for 72 h to form dense amorphous solids. The resulting amorphous solids were named Zr-*n*L_1, where *n* (4, 8, or 12) indicates the molar equivalent of succinic acid used during synthesis.

Sol-gel synthesis of amorphous Zr metal-organic frameworks with adipate linker (Zr-*n*L_2)

The ZrOAc (60.0 mg), synthesized in the previous step, was dissolved in Milli-Q water (0.5 mL). The solution was added into an aqueous solution of adipic acid (4, 8, or 12 molar equivalents, 99%, Merck Life Science BV) and Milli-Q water (4.5 mL) in a 22-ml glass vial. The vial was then capped and heated in a preheated oven at 80 °C for 72 h to ensure gelation equilibrium was reached. Cross-linking results in gel phases. The gels were then washed with Milli-Q water (20 mL) for 4 cycles, followed by solvent exchange with fresh ethanol (99.8%, Acros Organics NV), then dried at 80 °C for 72 h to form dense amorphous solids. The resulting amorphous solids were named Zr-*n*L_2, where *n* (4, 8, or 12) indicates the molar equivalent of adipic acid used during synthesis.

Sol-gel synthesis of Zr amorphous Zr metal-organic frameworks with thiomalate linker (Zr-*n*L$_3$)

The ZrOAc (60.0 mg), synthesised in the previous step, was dissolved in Milli-Q water (0.5 mL). The solution was added into an aqueous solution of thiomalic acid (2, 4, 8, or 12 molar equivalents, 99%, TCI Europe NV, racemic mixture) and Milli-Q water (4.5 mL) in a 22-ml glass vial. The vial was then capped and heated in a preheated oven at 80 °C for 72 h to ensure gelation equilibrium was reached. Cross-linking results in gel phases. The gels were then washed with Milli-Q water (20 mL) for 4 cycles, followed by solvent exchange with fresh ethanol (99.8%, Acros Organics NV), then dried at 80 °C for 72 h to form dense amorphous solids. The resulting amorphous solids were named Zr-*n*L$_3$, where *n* (2, 4, 8, or 12) indicates the molar equivalent of thiomalic acid used during synthesis.

Synthesis of amorphous Zr metal-organic frameworks with sulfosuccinate linker (Zr-*n*L$_4$)

The ZrOAc (60.0 mg), synthesised in the previous step, was dissolved in Milli-Q water (0.5 mL). The solution was added into an aqueous solution of thiomalic acid (2, 4, 8, or 12 molar equivalents, 99%, TCI Europe NV) and Milli-Q water (4.5 mL) in a 22-ml glass vial. The vial was then capped and heated in a preheated oven at 80 °C for 72 h to ensure gelation equilibrium was reached. Cross-linking results in gel phases. The gels were then washed with Milli-Q water (20 mL) for 4 cycles.

The thiol-functionalised gels were then oxidised with a 35% H_2O_2 solution (soaking, 20 mL, Chemsolute BV) for 2 h at room temperature. Then wash with Milli-Q water (20 mL) for 4 cycles. After removing water by decanting, 0.02 M H_2SO_4 (20 mL) was added to the oxidised gels and kept at room temperature for 30 min to fully protonate the sulfonate group. The resultant gels were then washed with Milli-Q water (20 mL) for 5 cycles, exchanged with fresh ethanol, and then dried at 80 °C for 72 h to form dense amorphous solids. The resulting amorphous solids were named Zr-*n*L$_4$, where *n* (2, 4, 8, or 12) indicates the molar equivalent of thiomalic acid used during synthesis.

Powder X-ray diffraction (PXRD)

Powder X-ray diffraction (PXRD) patterns were collected using a Malvern PANalytical Empyrean with a CuKα anode (45 kV, 50 mA). Samples were mounted on a high-throughput sample holder and measured in the 2θ range of 5° to 40° with a step size of 0.013°.

Synchrotron PXRD and X-ray total scattering

Each sample was filled into a Lindemann glass capillary with a diameter of 1 mm and flame-sealed. The synchrotron PXRD and X-ray total scattering of ZrOAc, Zr-4L$_1$, Zr-4L$_2$, Zr-4L$_3$, and Zr-4L$_4$ were collected on the BL04B2 beamline at the Super Photon ring-8 GeV (SPring-8, Hyogo,

Japan). The energy of the incident beam is 112.9232 keV (λ = 0.109795 Å). The exposure time is 600 s. The collected scattering data was subjected to absorption, background, and Compton scattering corrections, then normalised to give the Faber−Ziman total structure factor S(Q). The pair distribution function was calculated by Fourier transforming the S(Q) with a Lorch modification function.[2-4]

X-ray total scattering of MOF-801 and UiO-66 was collected on the ID11 beamline at the European Synchrotron Radiation Facility (ESRF, Grenoble, France). Each sample was filled into a Lindemann glass capillary with a diameter of 0.5 mm and flame sealed.

Extended X-ray absorption fine-structure (EXAFS)

Each sample was mixed with boron nitrile and pressed into pellets with a diameter of 10 mm and a thickness of 0.5 mm. The pellets were then sealed with plastic film. The synchrotron X-ray absorption spectra in the energy region of the Zr K-edge were collected in transmission mode on the BL14B2 beamline at the Super Photon ring-8 GeV (SPring-8, Hyogo, Japan). Fourier transformation was *k*2-weighted in the *k* range of 3.0 to 16 $Å^{-1}$. The data processing and fitting were performed using Athena and Artemis software.

Scanning electron microscopy (SEM)

Scanning electron microscope (SEM) images were taken using a Hitachi SU8000 instrument after platinum vapour deposition for 10 s. Note that Zr-$4L_3$ and Zr-$4L_4$ are electron beam sensitive, which limited SEM imaging at higher magnifications.

Thermogravimetric and calorimetric analysis

Thermalgravimetric analysis (TGA) results were obtained using a Netzsch STA 449F3 Jupiter with a heating rate of 10 °C min^{-1} under flowing N_2 (50 mL/min). TGA under air were obtained using Rigaku Thermo plus EVO2 TG-DTA8122 with a heating rate of 10 °C min^{-1} under flowing air (100 mL/min). The measurements were conducted in Al pans from 30 to 500 °C and Pt pans from 30 to 700 °C.

Differential Scanning Calorimetry (DSC) was collected using the Hitachi-Hitech DSC7000X under a flowing N_2 atmosphere. Note that samples were dehydrated at 200 °C prior to measurement to eliminate heat flows originated from the dehydration of interstitial water molecules.

^{1}H NMR

Samples were prepared by weighing 2 mg into a 1.5-mL vial. A 750-µL portion of the digestion medium was then added to the tube. The digestion medium used in this work was 10% NaOD in D_2O, using TMSP (trimethylsilylpropanoic acid) as a reference. The vials were capped and inverted 2−3 times before leaving the samples to digest overnight. This OH-based procedure dissolves only the organic portion of the system, and the inorganic component precipitates as ZrO_2. Afterwards, the clear supernatant solution was transferred to an NMR tube, and liquid ^{1}H NMR spectra were recorded at room temperature with 32 scans on a 400 MHz JEOL NMR spectrometer with a magnetic field strength of 14.1 Tesla. The relaxation delay (T_1) was set to 15 s to ensure that reliable integrals were obtained, allowing for the accurate determination of the relative concentrations of the molecular components. The number of scans was 32. Chemical shifts (δ) are given in ppm relative to D_2O (δ = 4.65 ppm for ^{1}H NMR).

X-ray photoelectron spectroscopy

X-ray photoelectron spectroscopy (XPS) results were collected using a PHI5600 Versaprobe III (Physical Electronics) utilising an aluminum Kα monochromatic X-ray source (1486.6 eV photon energy) with a beam irradiation power of 25 W.

High-resolution scans of the Zr 3d and S 2p photoelectron peaks were recorded from a spot diameter of 100 mm using a pass energy of 26 eV and a step size of 0.1 eV. Measurements were performed with a takeoff angle of 45° with respect to the sample surface. The vacuum in the analysis chamber was approximately 9×10^{-7} Pa during measurements. The powders were applied on scotch tape. The energy scale of the XPS spectra was calibrated relative to the binding energy of Zr 3d5/2 (182.6 eV) in $Zr(IV)O_2$.

The analysis and fitting were performed using CasaXPS software (Casa Software, Ltd.), employing a mixed Gaussian-Lorentzian peak shape and a Shirley-type background. The S $2p_{3/2}$ – $2p_{1/2}$ doublet separation is 1.18 eV, with peaks constrained to a 2:1 area ratio.

Protonic conductivity

Conductivity measurements were performed using the electrochemical impedance spectroscopy (EIS) technique. Samples were pressed into pellets with a diameter of 5 mm and a thickness between 0.4 and 0.5 mm. The pellets were then sandwiched between two gold-coated electrodes. All measurements were performed in a temperature- and humidity-controlled environment using an ESPEC SH-221 temperature and humidity chamber. The measurements were collected using a BioLogic SP-300 potentiostat over a frequency range of 1 MHz to 0.1 Hz with an input voltage amplitude of 100 mV. The collected data were analysed using EC-Lab software V11.33 via equivalent circuit fitting.

The ionic conductivity was calculated using the following equation:

$$\sigma = \frac{L}{(R) \times \pi r^2}$$

L represents the thickness of the pellet, *R* is the resistance, and *r* is the pellet radius.

Gas sorption

N_2 (77 K) adsorption/desorption isotherms were collected using BELSORP-mini volumetric adsorption equipment. Before the measurement, all samples were ground and activated at 130 °C for 12 h under vacuum.

Positron Annihilation Lifetime Spectroscopy (PALS)

PALS experiments were conducted using PSA TypeL-II (Toyo Seiko) equipped with a Na-22 positron source. Non-activated samples were positioned in the center of a stainless-steel holder capped with Kapton film. Lifetimes were measured with a target integrated count of 10^6 and analysed using IPALM version 2.4 software.

Hardness

Hardness with a standard triangular pyramid indenter with a 115° tip angle (DHT115) results were obtained using a SHIMADZU Dynamic Ultra-micro Hardness Tester DUH-211. The maximum load is limited to 10 mN and held for 5 sec before releasing the load. The indentation speed is set to 0.2926 mN/sec. Hardness is obtained based on the load value and the indentation depth during the loading process:

$$\text{HT115 (GPa)} = 0.16007 \times F_N/h^2$$

F_N and h are test force (mN) and indentation depth (μm), respectively.

Supplementary figures

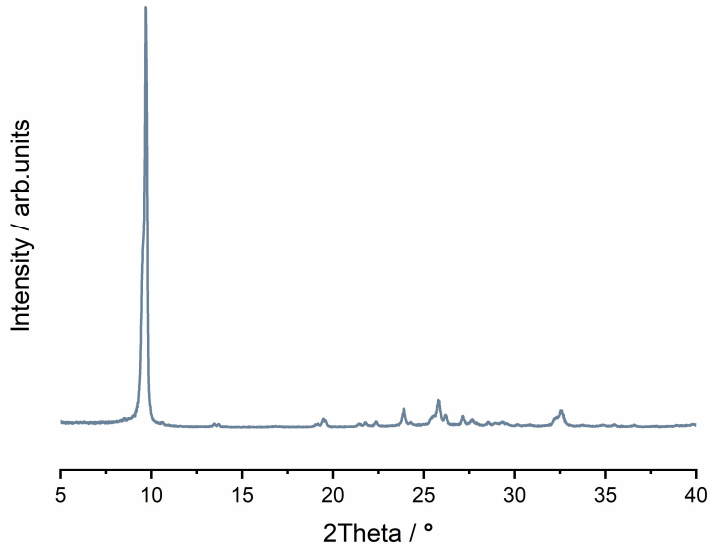

Fig. S1. PXRD patterns of ZrOAc cluster matched with the ref. 1 of ESI.

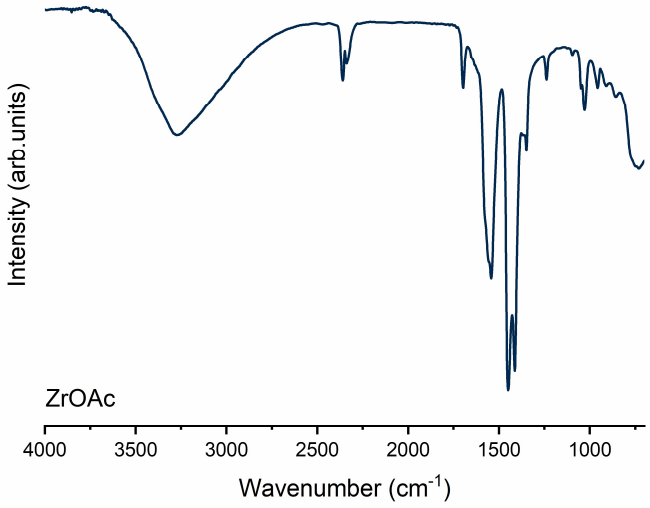

Fig. S2. FTIR of the as-synthesised ZrOAc cluster.

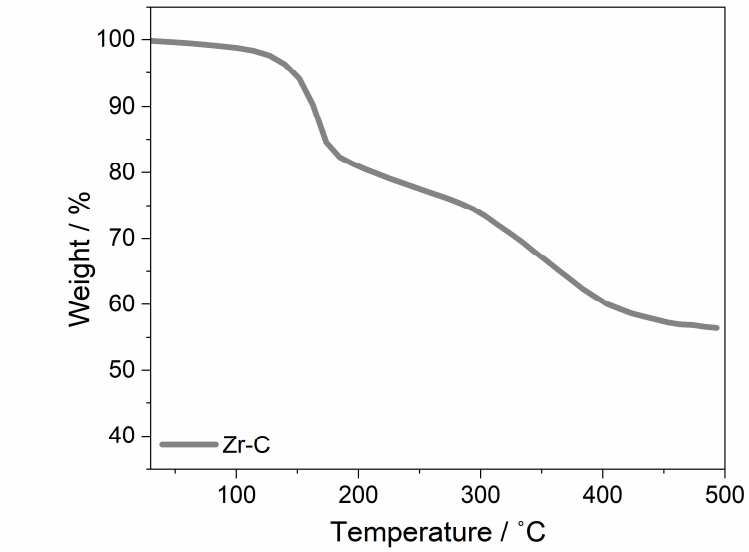

Fig. S3. TGA of the as-synthesised ZrOAc cluster.

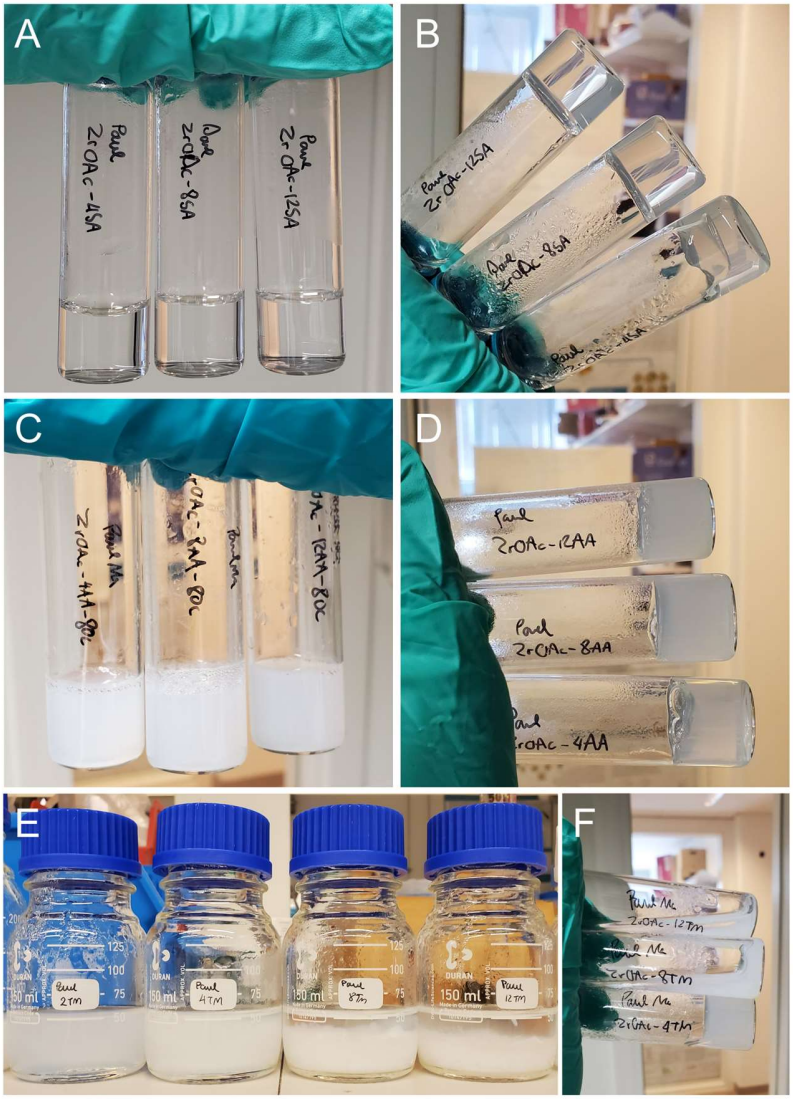

Fig. S4. Cross-linked gels synthesised from ZrOAc with (A, B) succinic acid (L_1) n = 4, 8, and 12, (C, D) adipic acid (L_2) n = 4, 8, and 12, (E) thiomalic acid (L_3) n = 2, 4, 8, and 12, and thiomalic acid (L_3) n = 4, 8, and 12. Note that the reaction between ZrOAc and L_3 is relatively fast, hindering monolithic gel formation for n > 4. n represents the molar equivalent of ligands used during the cross-linking process.

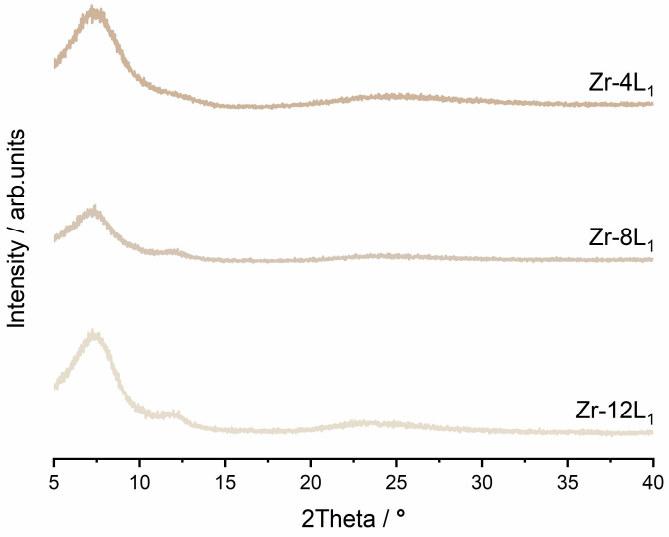

Fig. S5. PXRD (λ = 1.5406 Å) of Zr-4L_1, Zr-8L_1, and Zr-12L_1.

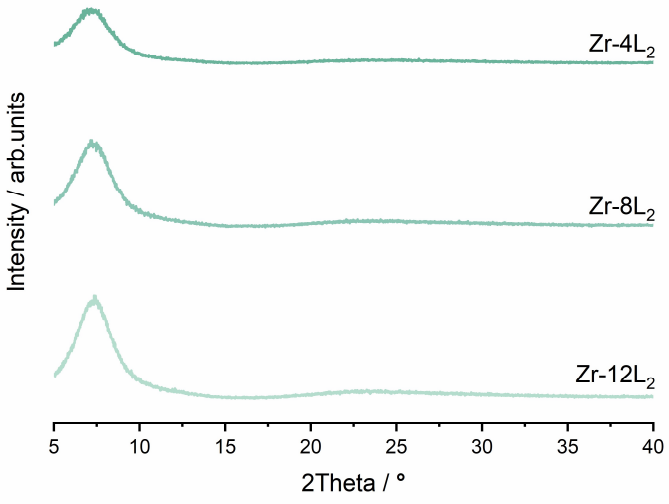

Fig. S6. PXRD (λ = 1.5406 Å) of Zr-4L_2, Zr-8L_2, and Zr-12L_2.

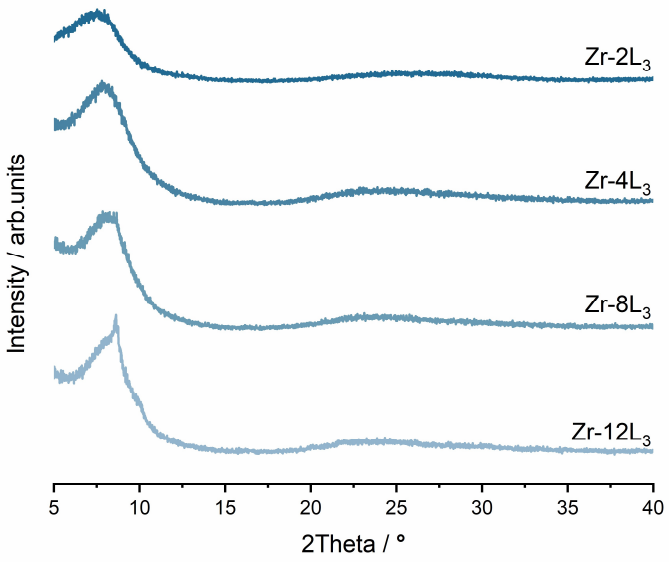

Fig. S7. PXRD (λ = 1.5406 Å) of Zr-2L_3, Zr-4L_3, Zr-8L_3, and Zr-12L_3.

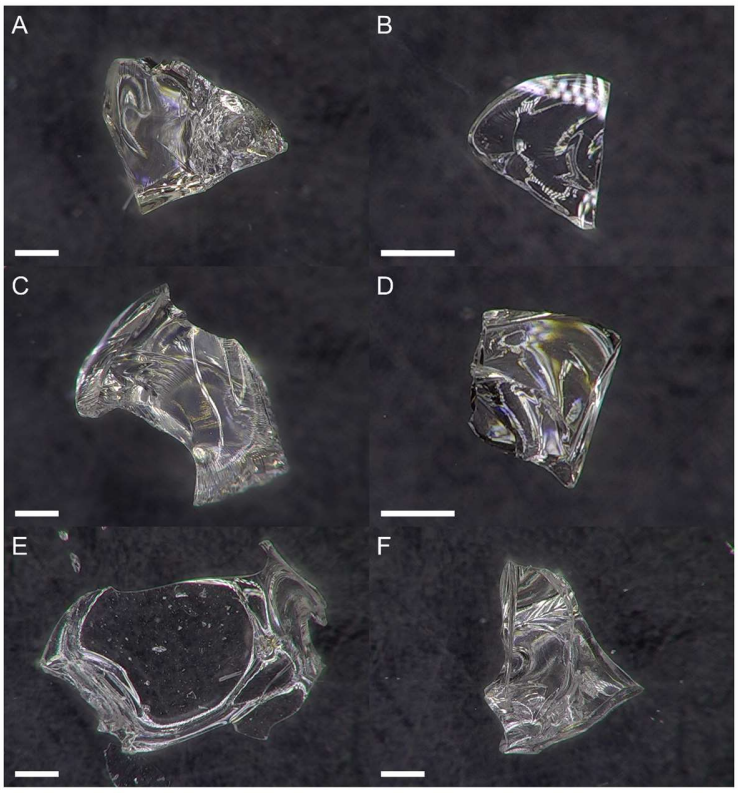

Fig. S8. Optical images of (A, B) Zr-4L_1, (C, D) Zr-8L_1, and (E, F) Zr-12L_1. The scale bars = 0.5 mm.

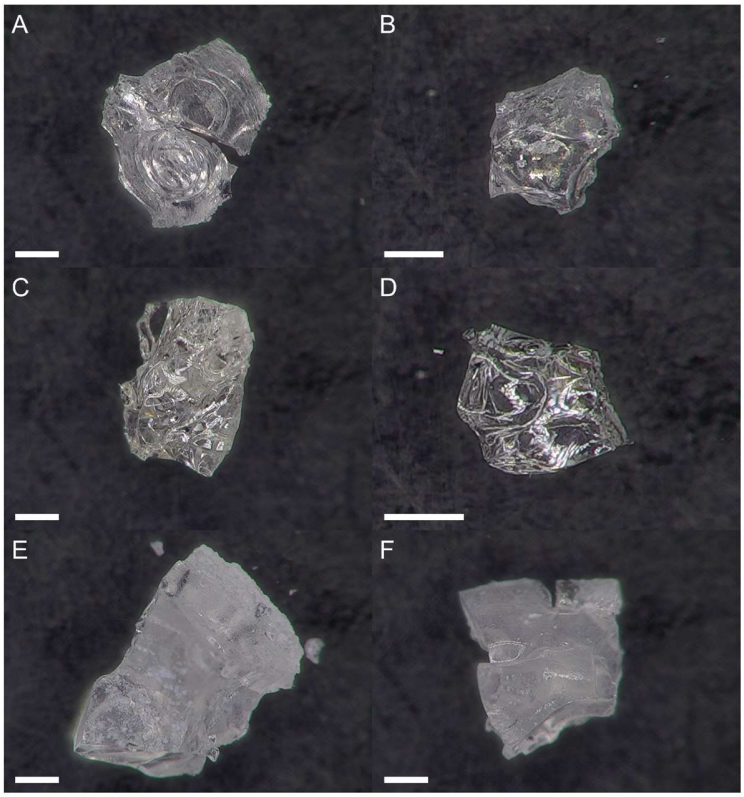

Fig. S9. Optical images of (A, B) Zr-4L_2, (C, D) Zr-8L_2, and (E, F) Zr-12L_2. The scale bars = 0.5 mm.

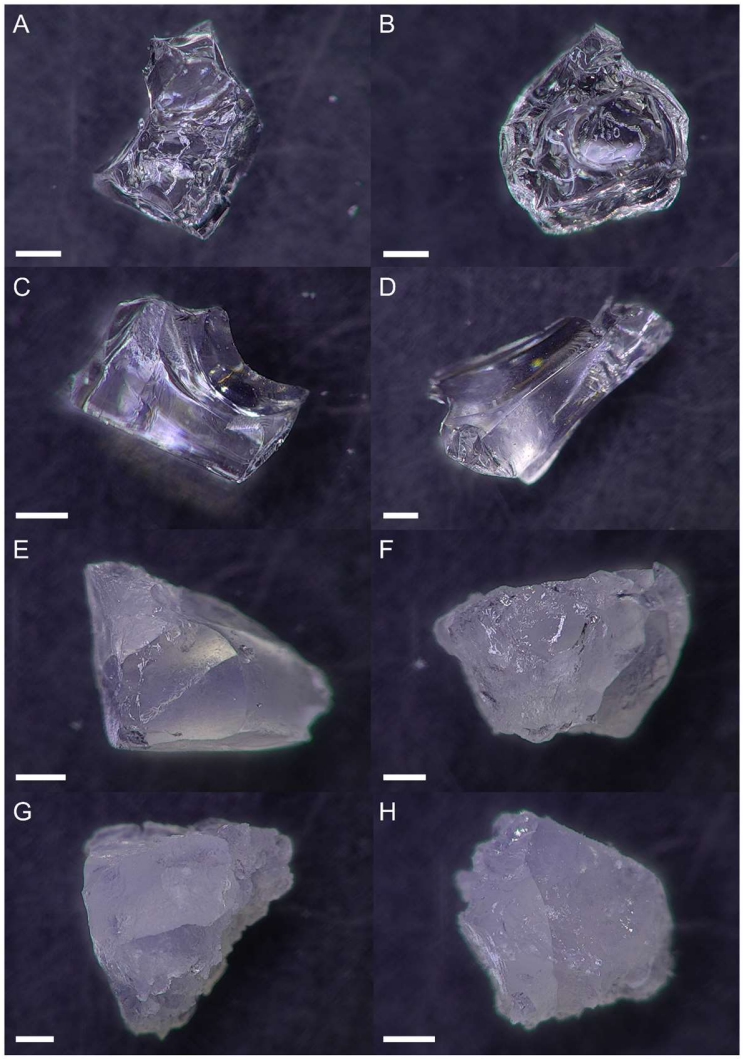

Fig. S10. Optical images of (A, B) Zr-2L_3, (C, D) Zr-4L_3, (E, F) Zr-8L_3, and (G, H) Zr-12L_3. The scale bars = 0.5 mm.

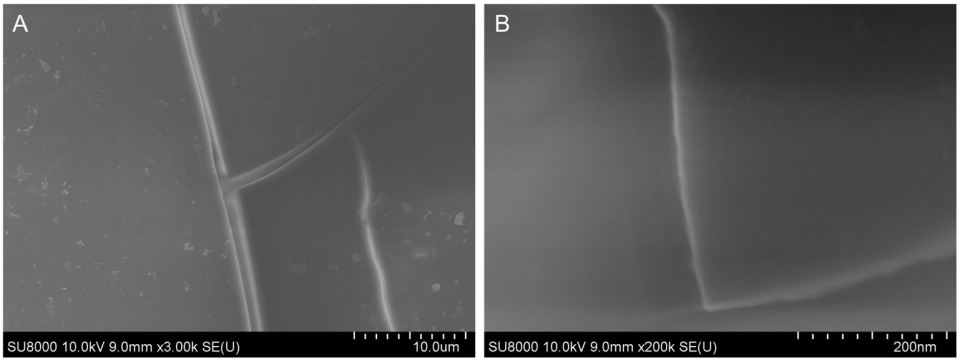

Fig. S11. SEM images of Zr-4L$_1$ at magnification of (A) x3k and (B) x200k.

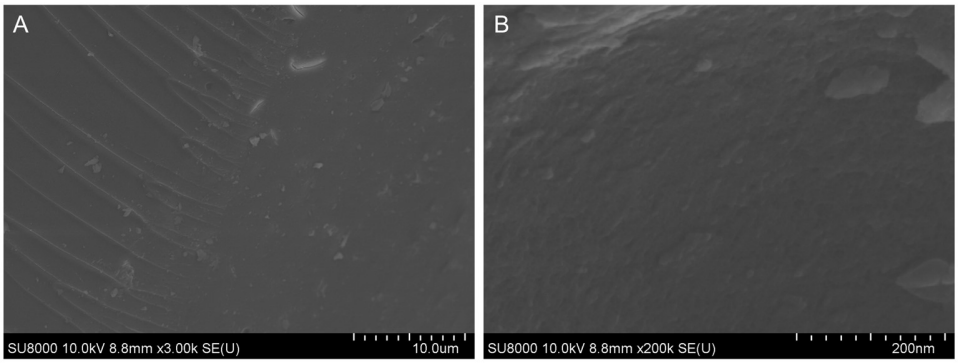

Fig. S12. SEM images of Zr-4L$_2$ at magnification of (A) x3k and (B) x200k.

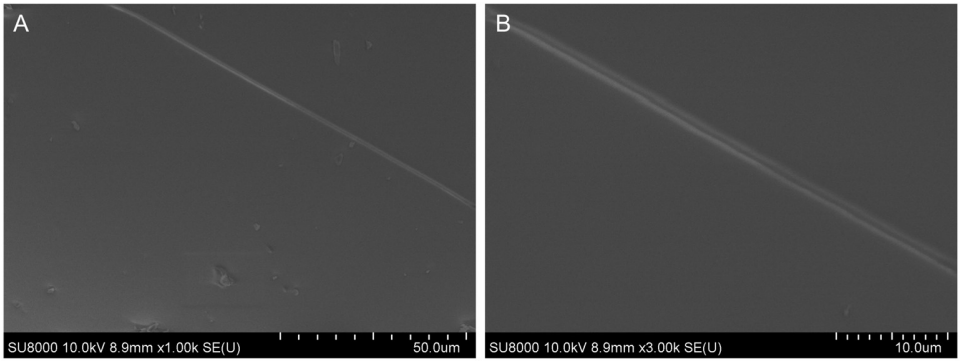

Fig. S13. SEM images of Zr-4L$_3$ at magnification of (A) x1k and (B) x3k.

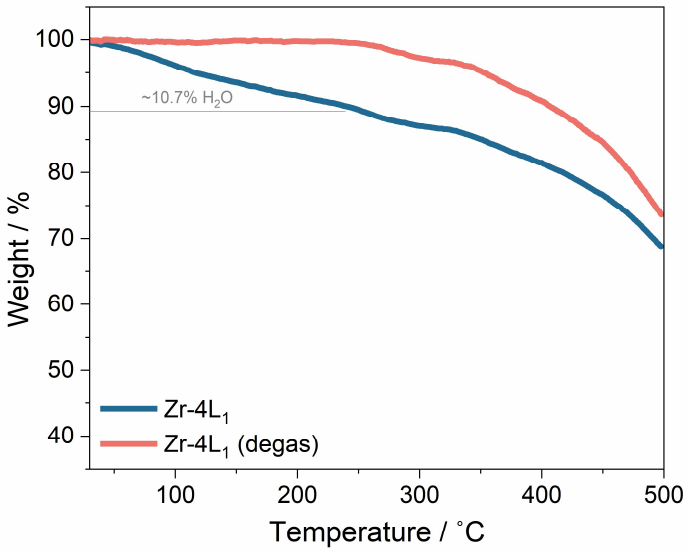

Fig. S14. TGA of Zr-4L$_1$ (blue) and Zr-4L$_1$ after degas at 200 °C (red). The measurements were conducted under N_2 flow (50 mL min^{-1}) with heating rate of 10 °C min^{-1}.

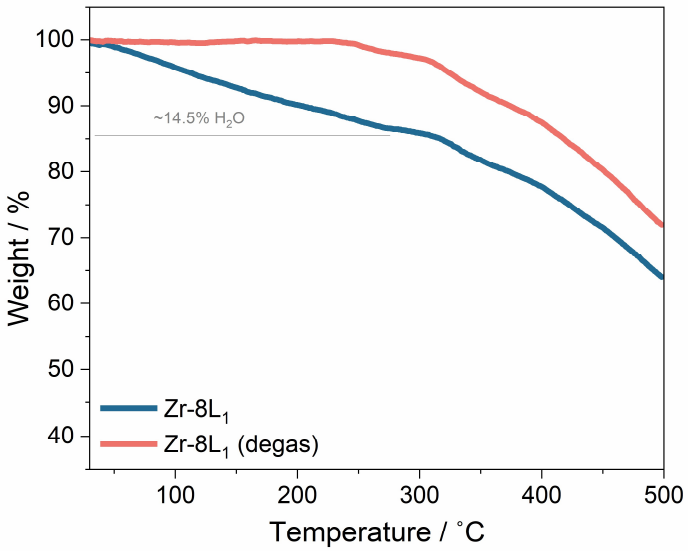

Fig. S15. TGA of Zr-8L$_1$ (blue) and Zr-8L$_1$ after degas at 200 °C (red). The measurements were conducted under N_2 flow (50 mL min^{-1}) with heating rate of 10 °C min^{-1}.

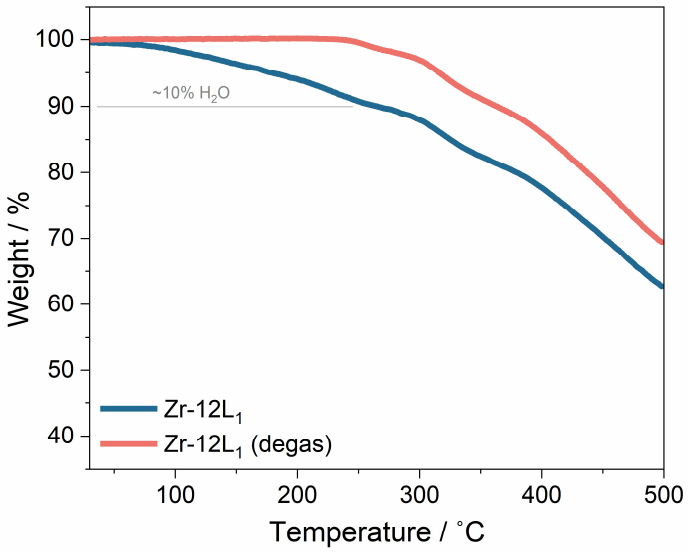

Fig. S16. TGA of Zr-12L_1 (blue) and Zr-12L_1 after degas at 200 °C (red). The measurements were conducted under N_2 flow (50 mL min^{-1}) with heating rate of 10 °C min^{-1}.

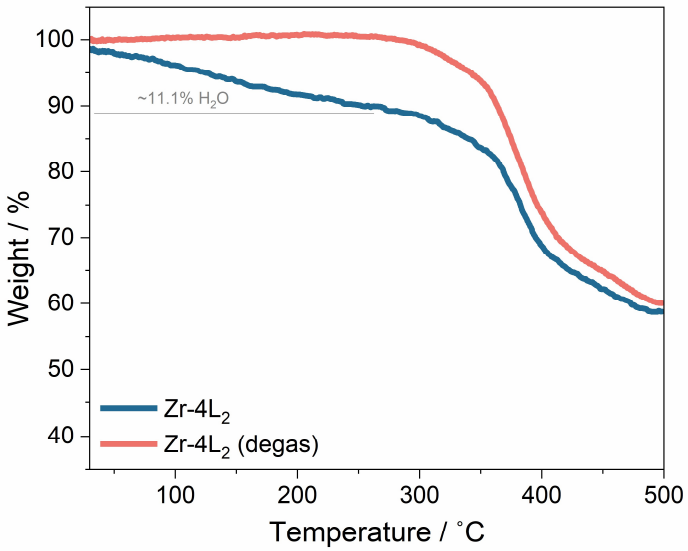

Fig. S17. TGA of Zr-4L_2 (blue) and Zr-4L_2 after degas at 200 °C (red). The measurements were conducted under N_2 flow (50 mL min^{-1}) with heating rate of 10 °C min^{-1}.

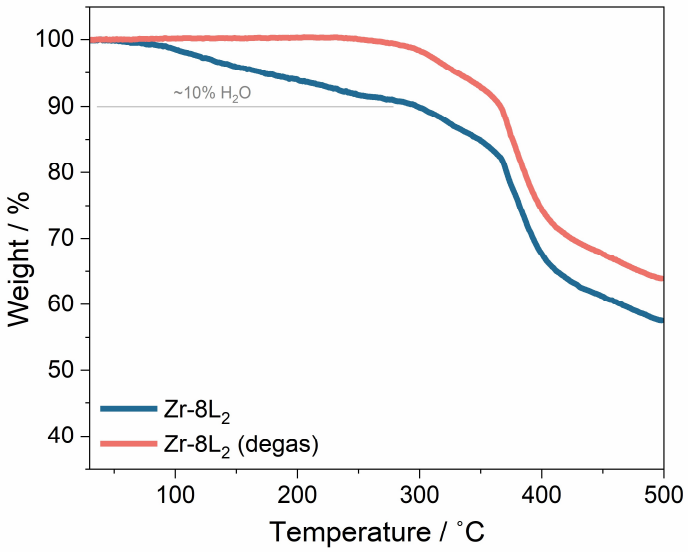

Fig. S18. TGA of Zr-8L_2 (blue) and Zr-8L_2 after degas at 200 °C (red). The measurements were conducted under N_2 flow (50 mL min^{-1}) with heating rate of 10 °C min^{-1}.

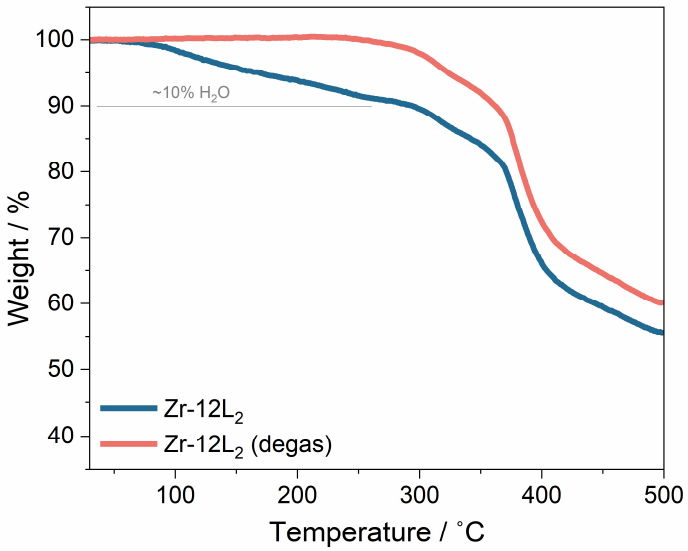

Fig. S19. TGA of Zr-12L_2 (blue) and Zr-12L_2 after degas at 200 °C (red). The measurements were conducted under N_2 flow (50 mL min^{-1}) with heating rate of 10 °C min^{-1}.

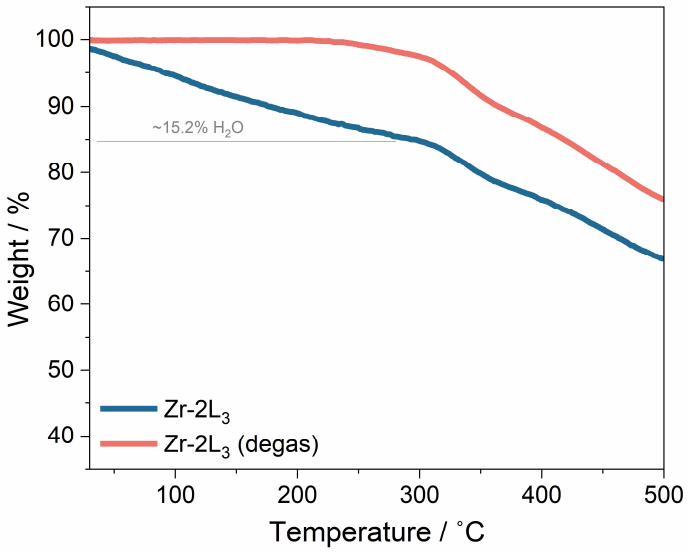

Fig. S20. TGA of Zr-2L_3 (blue) and Zr-2L_3 after degas at 200 °C (red). The measurements were conducted under N_2 flow (50 mL min^{-1}) with heating rate of 10 °C min^{-1}.

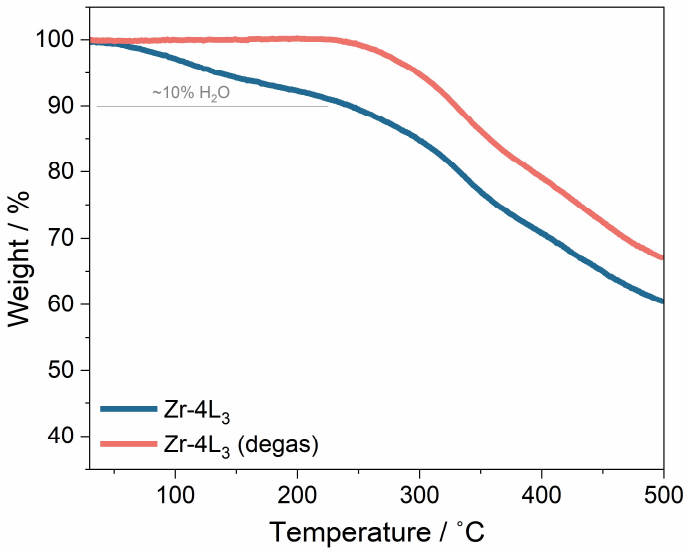

Fig. S21. TGA of Zr-4L_3 (blue) and Zr-4L_3 after degas at 200 °C (red). The measurements were conducted under N_2 flow (50 mL min^{-1}) with heating rate of 10 °C min^{-1}.

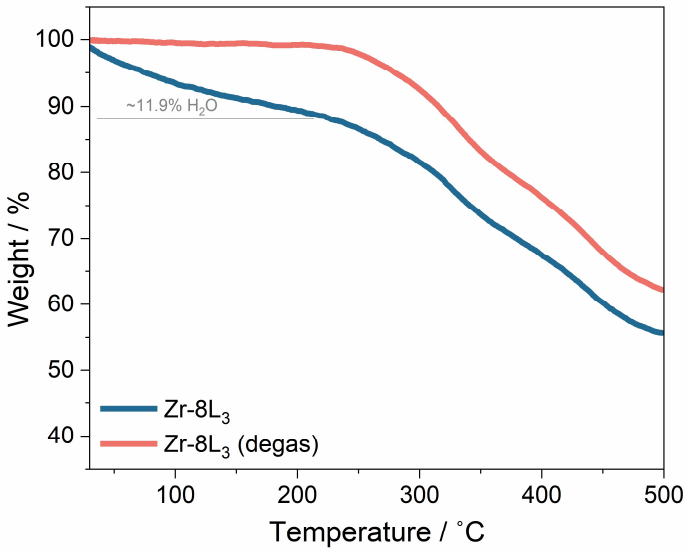

Fig. S22. TGA of Zr-8L_3 (blue) and Zr-8L_3 after degas at 200 °C (red). The measurements were conducted under N_2 flow (50 mL min^{-1}) with heating rate of 10 °C min^{-1}.

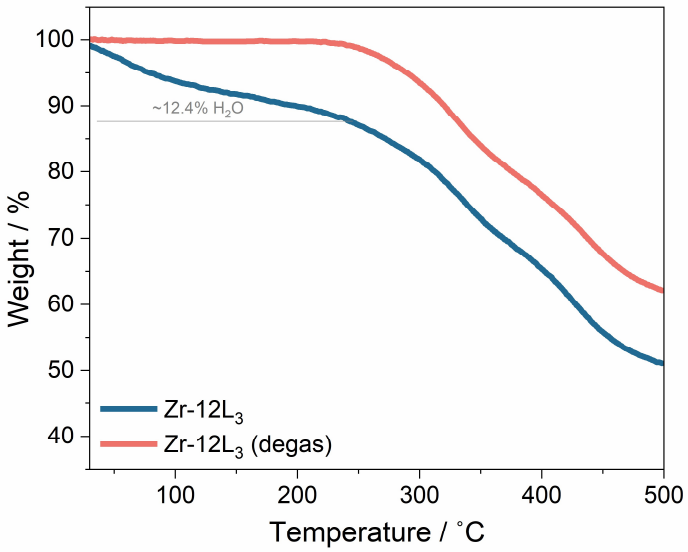

Fig. S23. TGA of Zr-12L_3 (blue) and Zr-12L_3 after degas at 200 °C (red). The measurements were conducted under N_2 flow (50 mL min^{-1}) with heating rate of 10 °C min^{-1}.

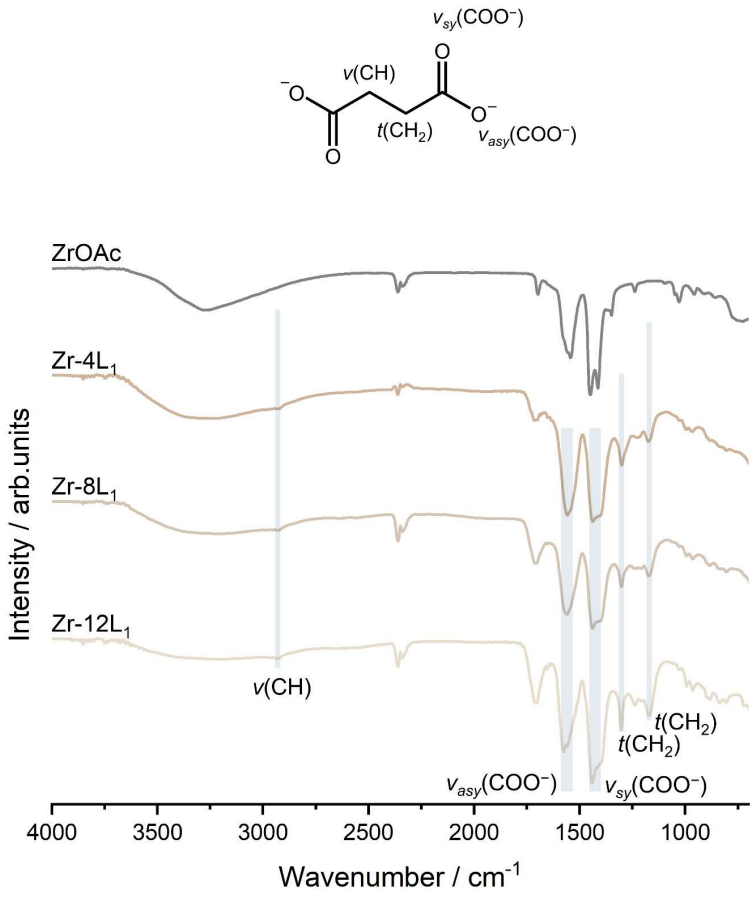

Fig. S24. FTIR of the ZrOAc cluster, Zr-4L$_1$, Zr-8L$_1$, and Zr-12L$_1$.

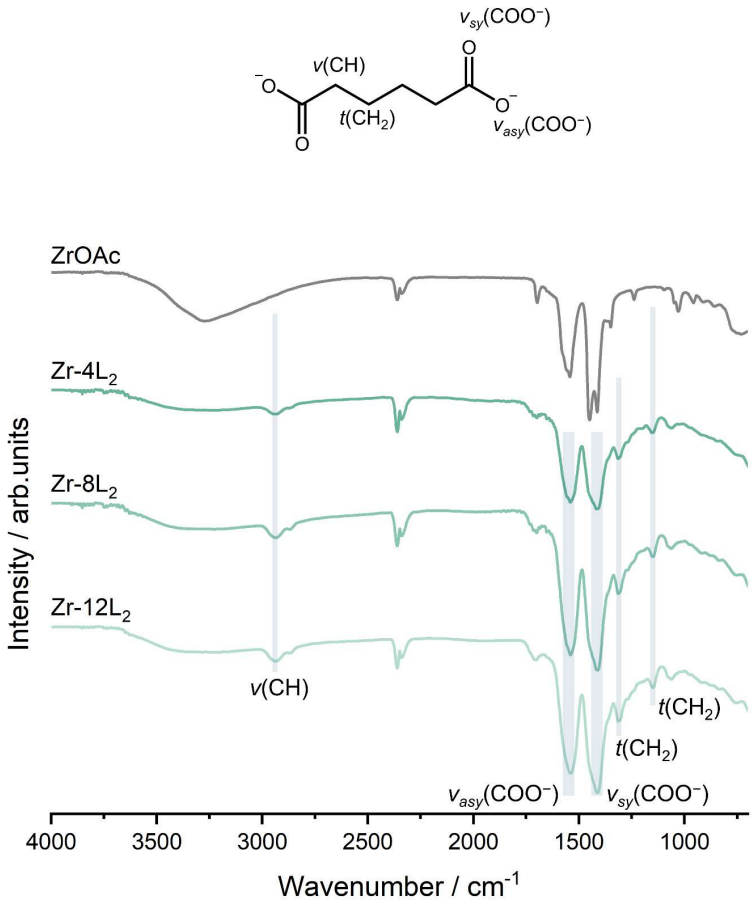

Fig. S25. FTIR of the ZrOAc cluster, Zr-4L$_2$, Zr-8L$_2$, and Zr-12L$_2$.

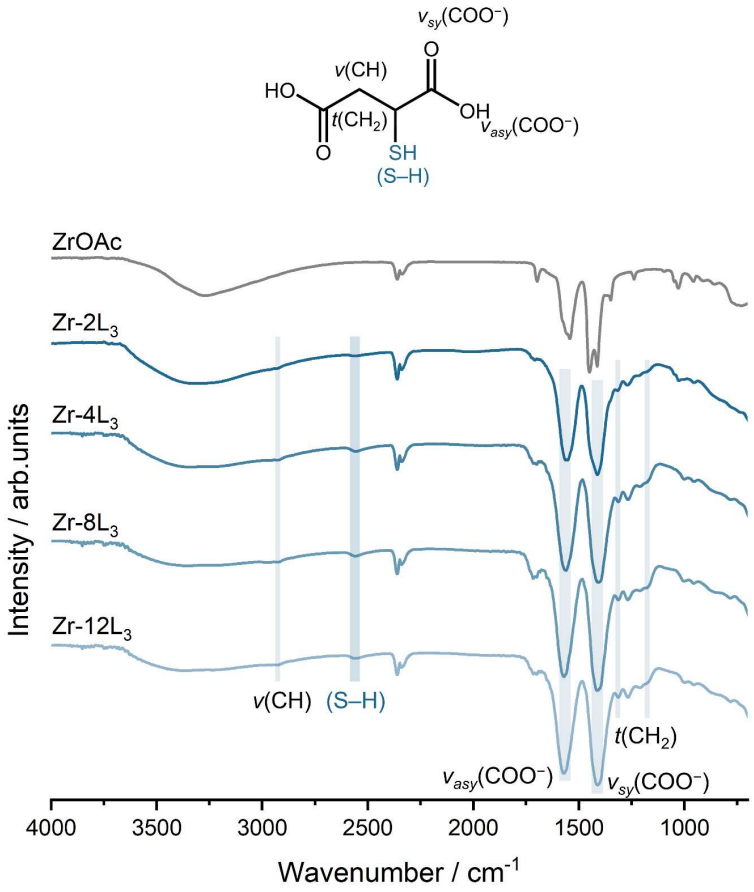

Fig. S26. FTIR of the ZrOAc cluster, Zr-2L$_3$, Zr-4L$_3$, Zr-8L$_3$, and Zr-12L$_3$.

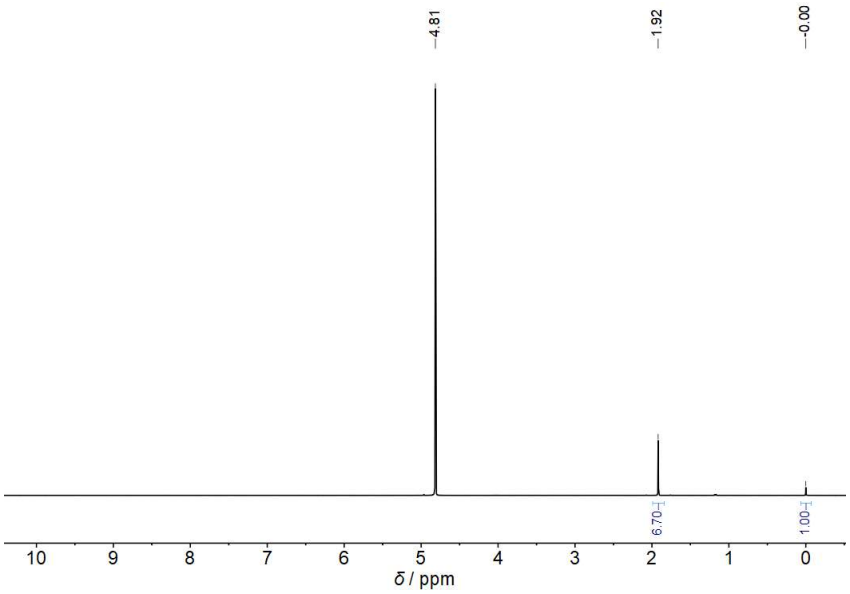

Fig. S27. ^{1}H NMR (400 MHz, D_2O) spectrum of ZrOAc.

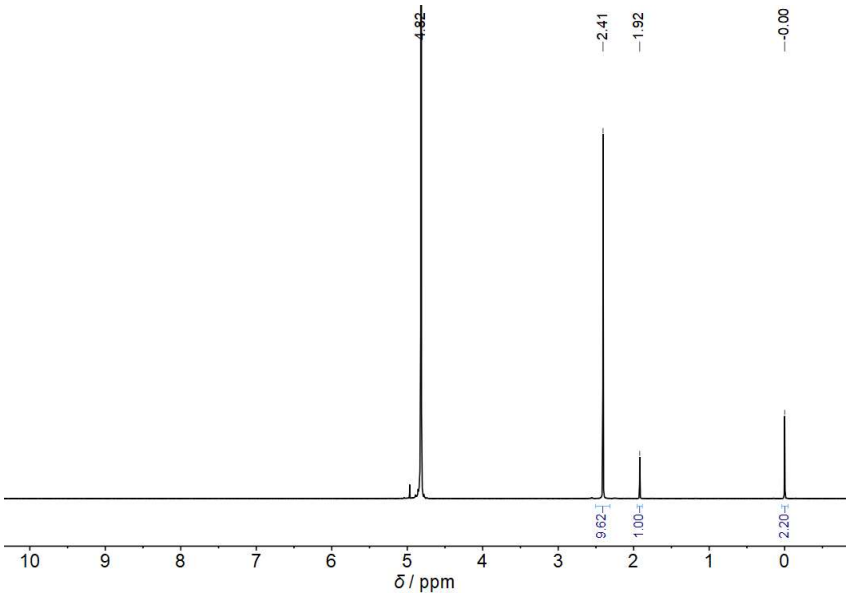

Fig. S28. ^{1}H NMR (400 MHz, D_2O) spectrum of Zr-4L_1.

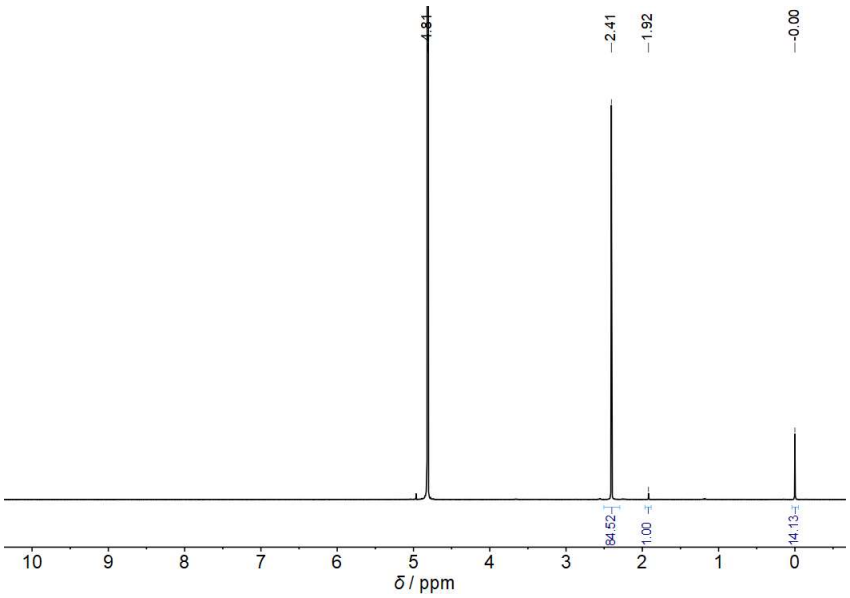

Fig. S29. ^{1}H NMR (400 MHz, D_2O) spectrum of Zr-8L_1.

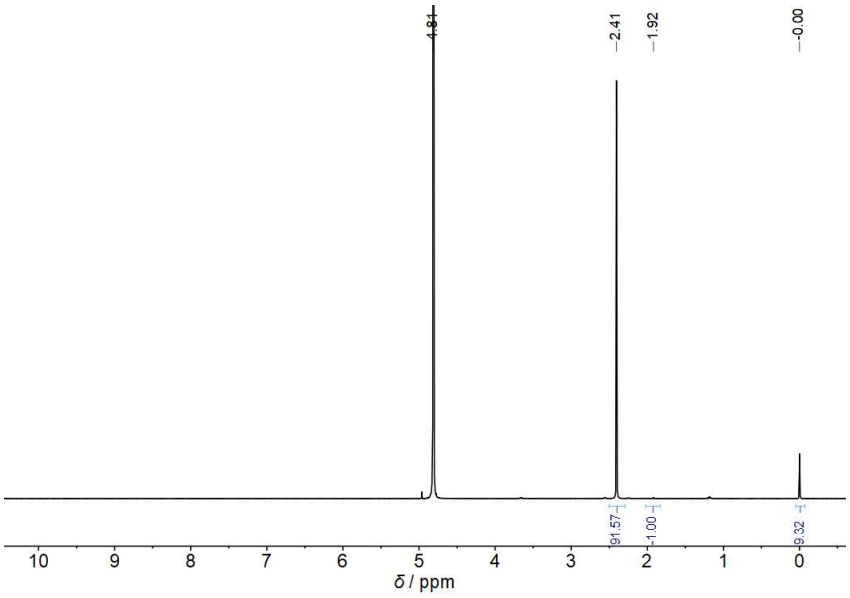

Fig. S30. ^{1}H NMR (400 MHz, D_2O) spectrum of Zr-12L_1. Peaks at ca. 1.2 and 3.7 ppm are from residual ethanol use during synthesis.

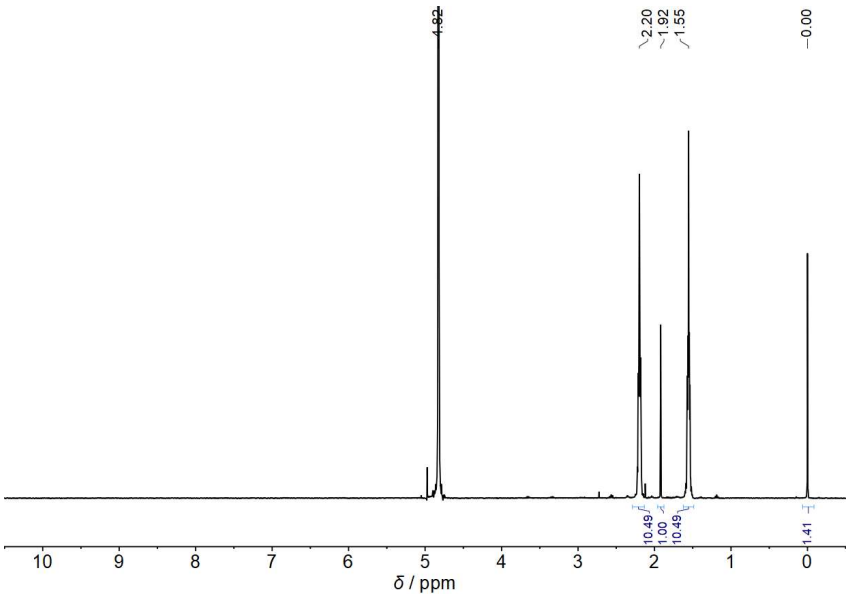

Fig. S31. ^{1}H NMR (400 MHz, D_2O) spectrum of Zr-4L_2. Peaks at ca. 1.2 and 3.7 ppm are from residual ethanol use during synthesis.

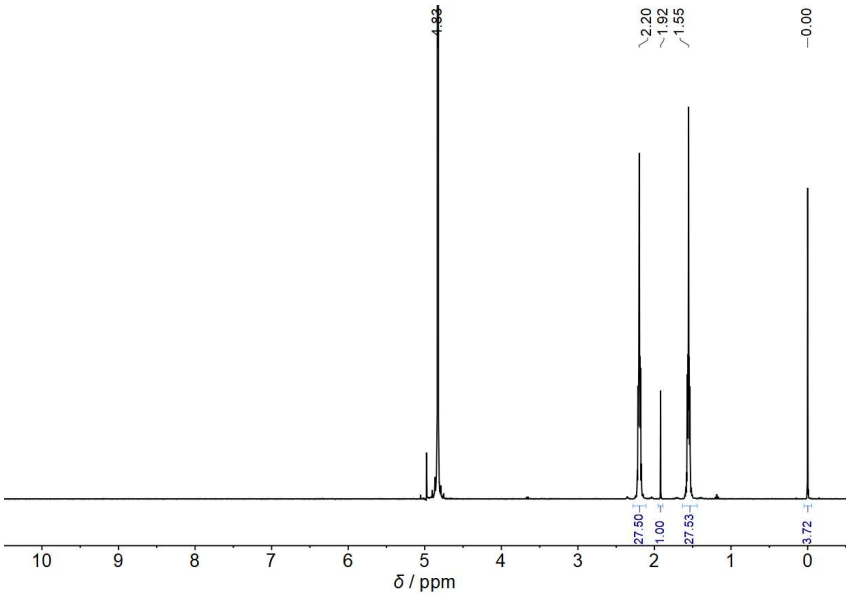

Fig. S32. ^{1}H NMR (400 MHz, D_2O) spectrum of Zr-8L_2. Peaks at ca. 1.2 and 3.7 ppm are from residual ethanol use during synthesis.

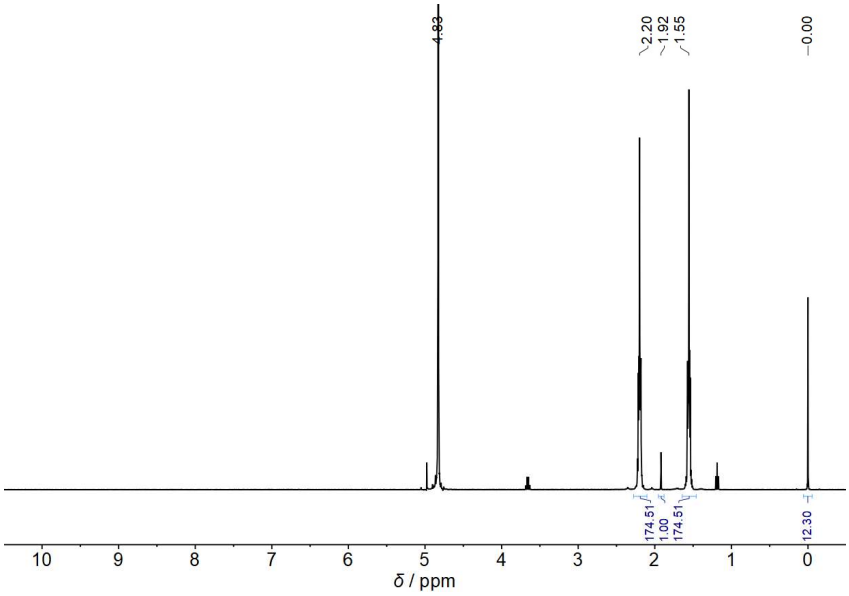

Fig. S33. ^{1}H NMR (400 MHz, D_2O) spectrum of Zr-12L_2. Peaks at ca. 1.2 and 3.7 ppm are from residual ethanol use during synthesis.

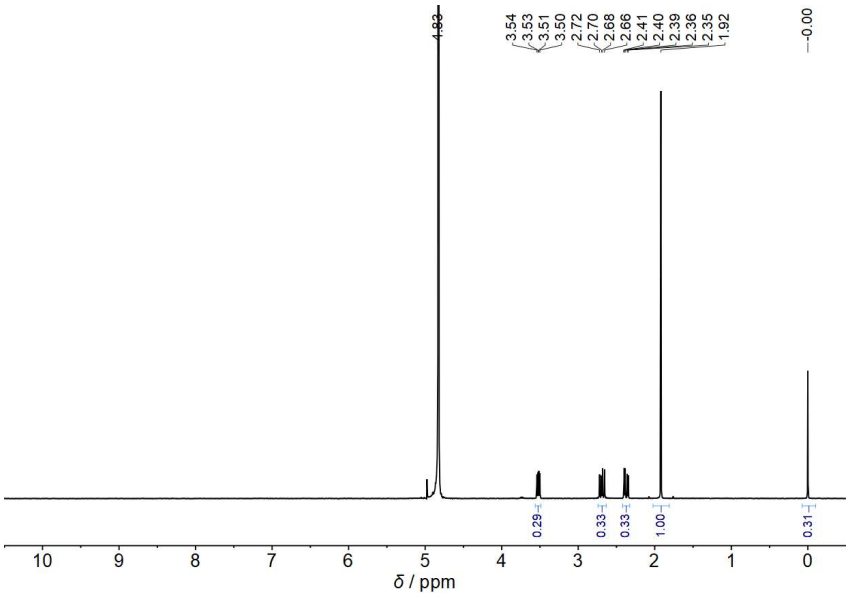

Fig. S34. ^{1}H NMR (400 MHz, D_2O) spectrum of Zr-2L_3.

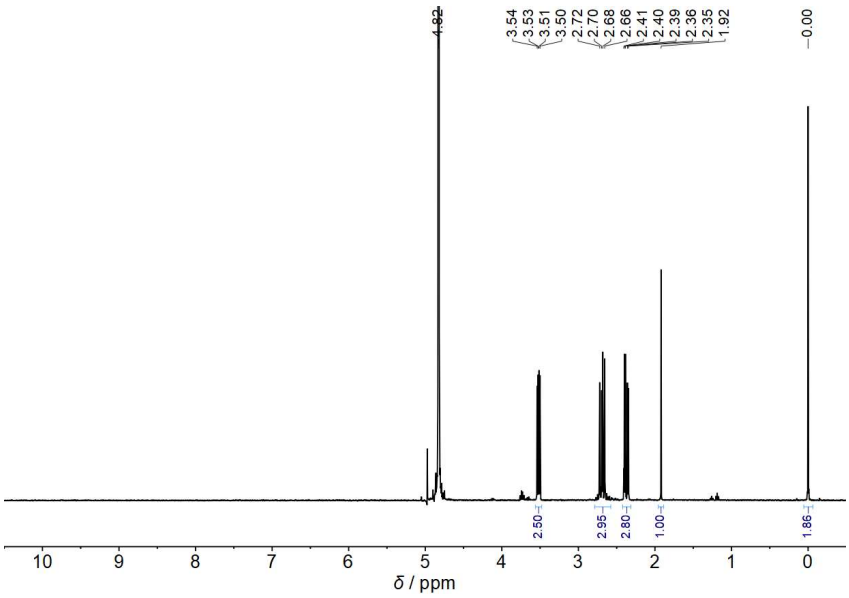

Fig. S35. ^{1}H NMR (400 MHz, D_2O) spectrum of Zr-4L_3. Peaks at ca. 1.2 and 3.7 ppm are from residual ethanol use during synthesis. Peaks at ca. 3.8 ppm correspond to ethyl esters formed during sample digestion.

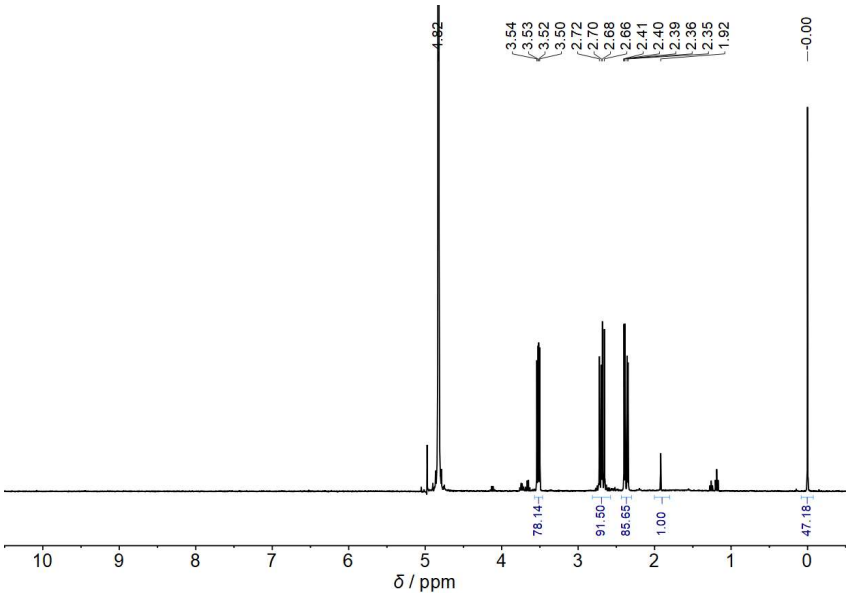

Fig. S36. ^{1}H NMR (400 MHz, D_2O) spectrum of Zr-8L_3. Peaks at ca. 1.2 and 3.7 ppm are from residual ethanol use during synthesis. Peaks at ca. 3.8 ppm correspond to ethyl esters formed during sample digestion.

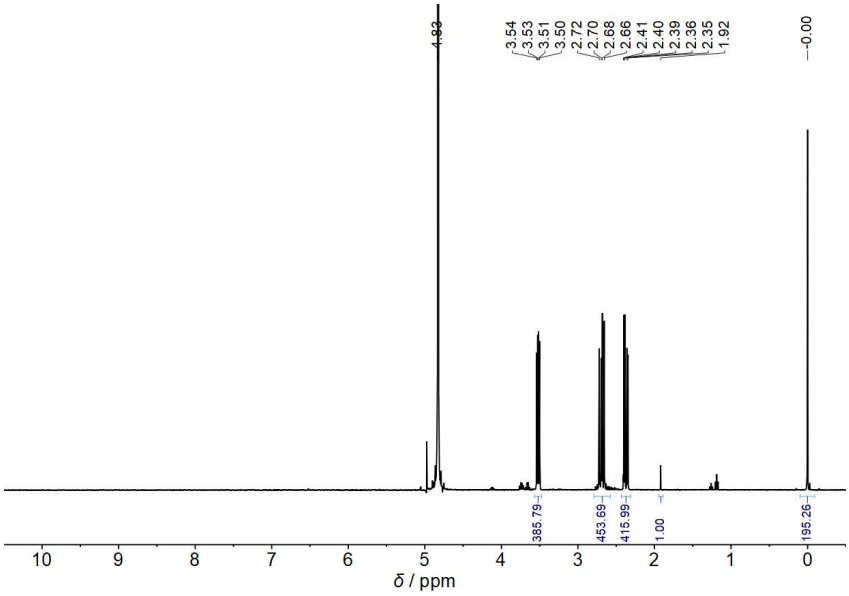

Fig. S37. ^{1}H NMR (400 MHz, D_2O) spectrum of Zr-12L_3. Peaks at ca. 1.2 and 3.7 ppm are from residual ethanol use during synthesis. Peaks at ca. 3.8 ppm correspond to ethyl esters formed during sample digestion.

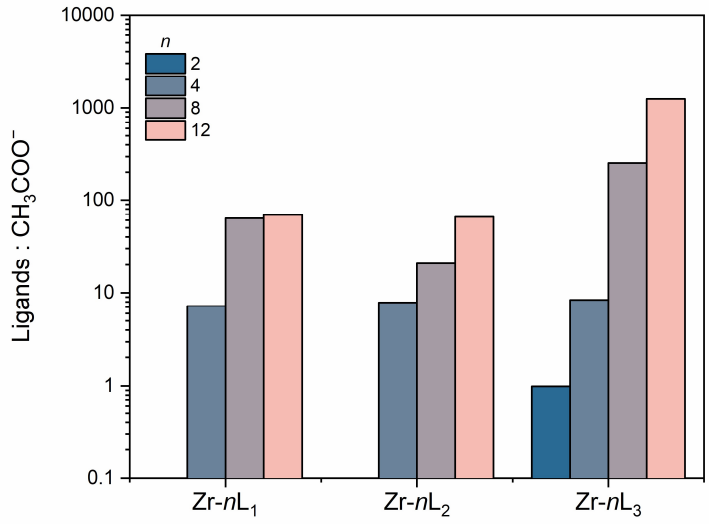

Fig. S38. Bidentate ligands to acetate ratios calculated from ^{1}H NMR results.

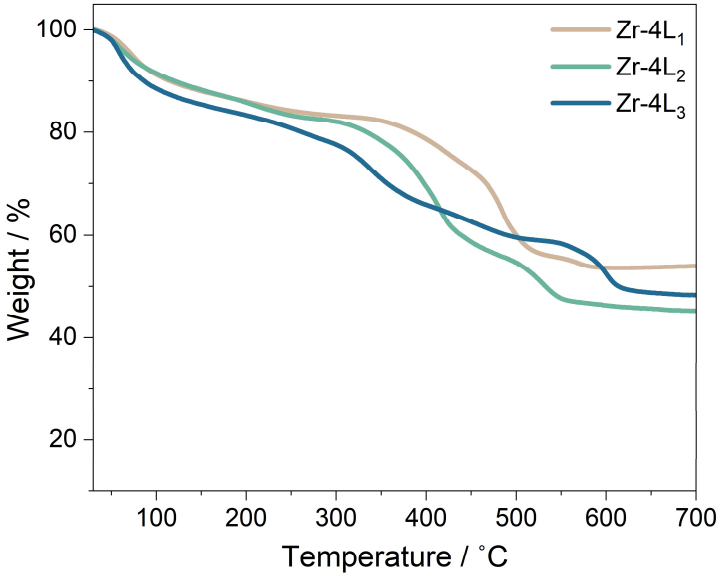

Fig. S39. TGA of Zr-4L_1 (beige), Zr-4L_2 (green), and Zr-4L_3 (blue) from 30 to 700 °C. The measurements were conducted under air flow (100 mL min^{-1}) with a heating rate of 10 °C min^{-1}. The bridging ligand contents are determined from weight loss between 285 °C and 700 °C for Zr-4L_1 and Zr-4L_2 and between 195 °C and 700 °C for Zr-4L_3.

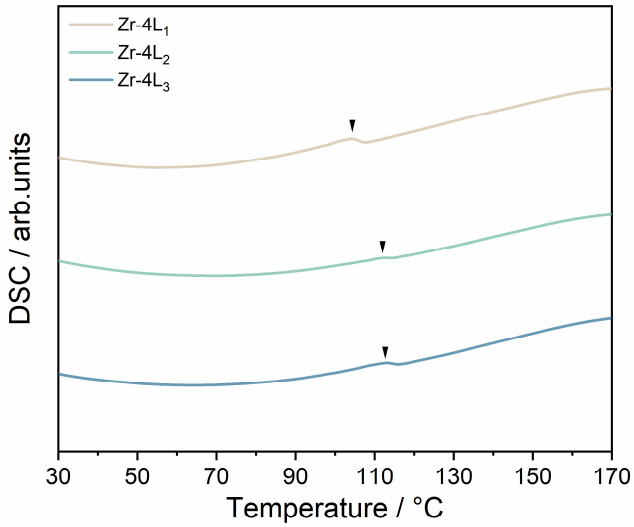

Fig. S40. DSC profiles of Zr-4L_1, Zr-4L_2, and Zr-4L_3 at the heating rate of 10 °C min^{-1}.

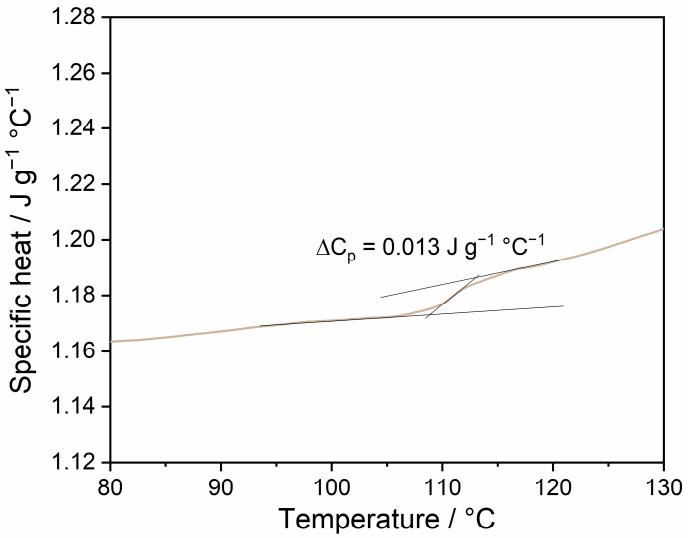

Fig. S41. Specific heat capacity measurement of Zr-4L$_1$ at the heating rate of 10 °C min^{-1} using a standard sapphire disk as a reference.

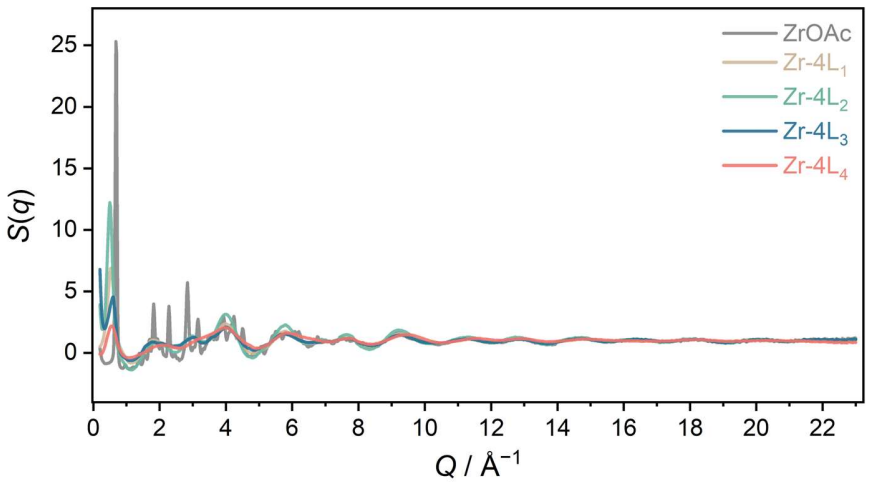

Fig. S42. *S*(*q*) of ZrOAc, Zr-4L$_1$, Zr-4L$_2$, Zr-4L$_3$, and Zr-4L$_4$.

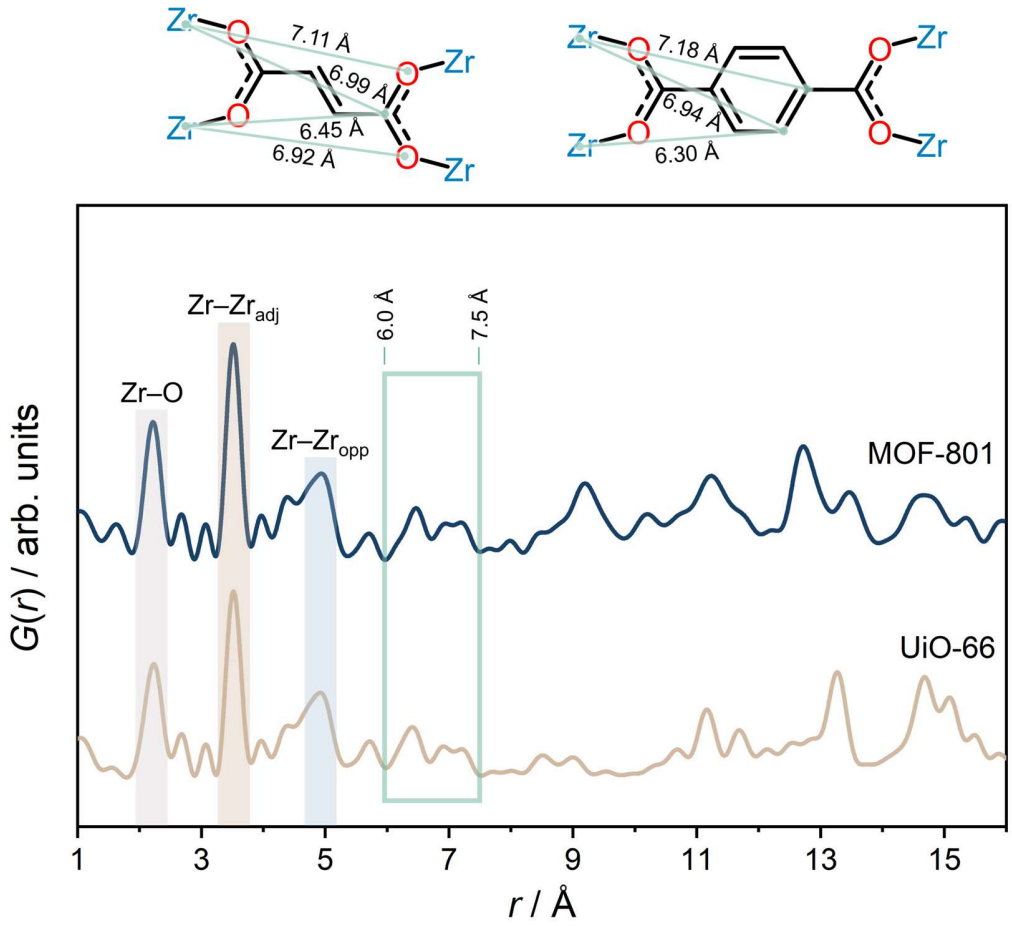

Fig. S43. Pair distribution function (PDF) results of MOF-801 and UiO-66 and PDF peak assignments (top). The displayed pair distances were measured from the crystal structures of MOF-801[5] and UiO-66.[6]

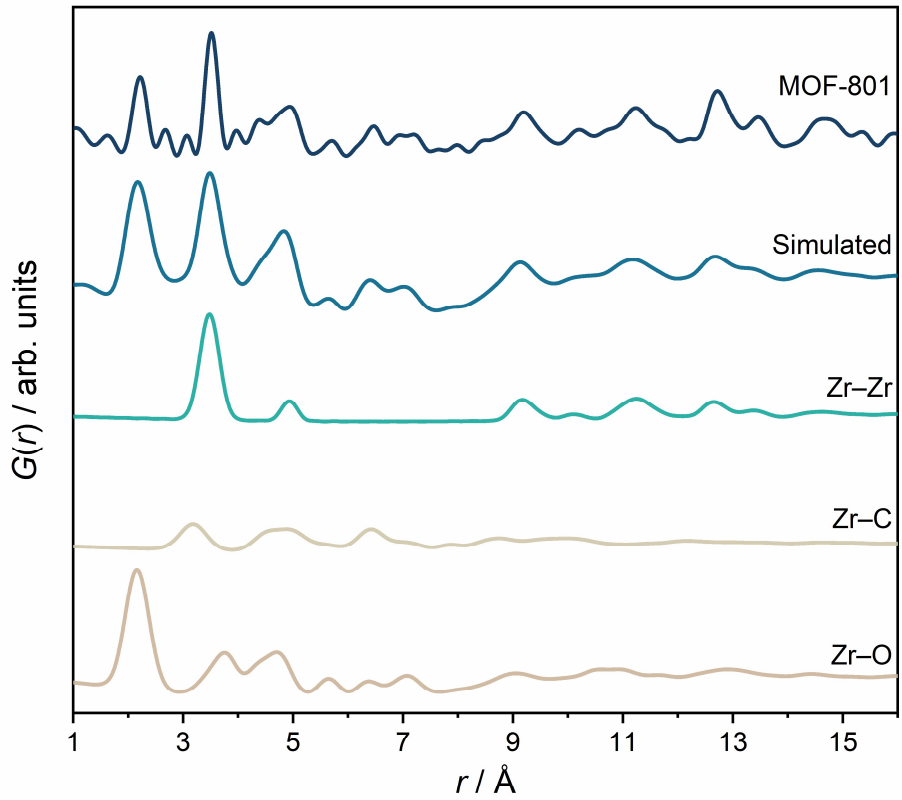

Fig. S44. Pair distribution function (PDF) results of MOF-801, simulated PDF of MOF-801, and simulated partial PDFs for Zr–Zr, Zr–C, and Zr–O pairs. The simulated PDFs were generated via PDFgui 2.0.3 software[7] using crystal structure MOF-801 from ref. [5].

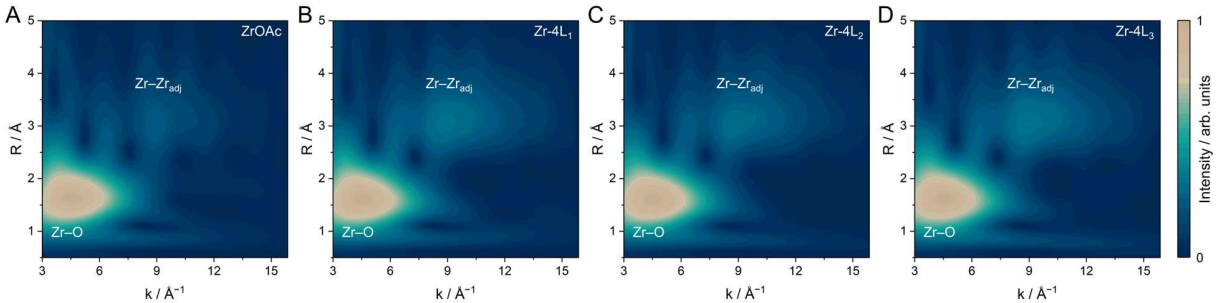

Fig. S45. Wavelet transform (WT) extended X-ray absorption fine structure (EXAFS) at the Zr-K edge of (F) ZrOAc, (G) Zr-4L_1, (H) Zr-4L_2, and (I) Zr-4L_3.

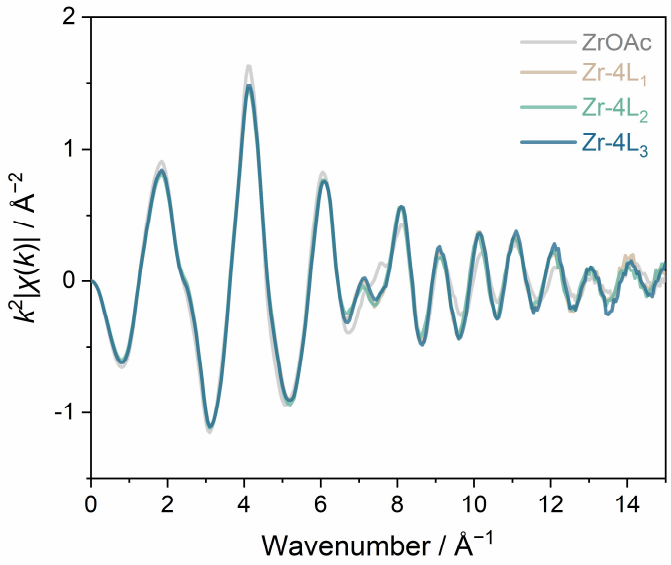

Fig. S46. Extended X-ray absorption fine structure (EXAFS) functions at Zr K-edge for ZrOAc, Zr-4L$_1$, Zr-4L$_2$, and Zr-4L$_3$.

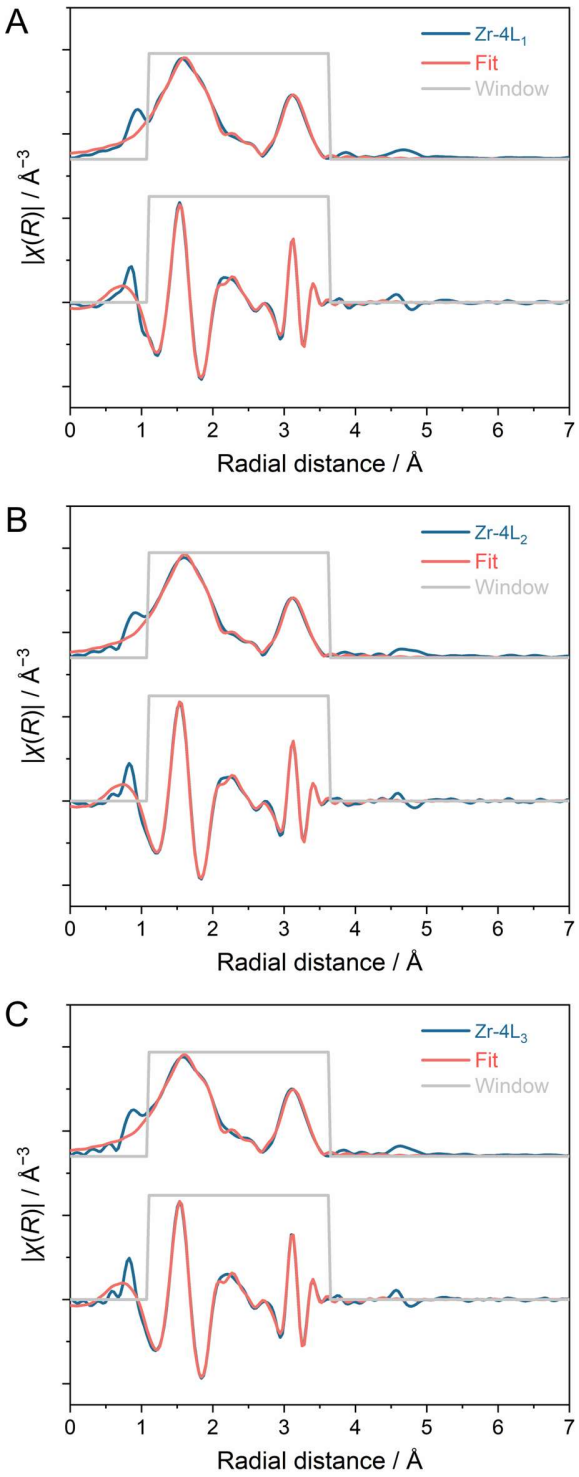

Fig. S47. Fourier transform (magnitude and real component) of the EXAFS at the Zr K-edge, with fitting curves for (A) Zr-4L_1, (B) Zr-4L_2, and (C) Zr-4L_3. The single crystal data of $Zr_6(O)_4(OH)_4(CH_3COO)_{12}\cdot 8.5H_2O$[8] was used as the initial model, and the fitted results are presented in Table S1.

Table S1. Zr K-edge EXAFS data fitting results of Zr-4L_1, Zr-4L_2, and Zr-4L_3. The R-factor of Zr-4L_1, Zr-4L_2, and Zr-4L_3 are 0.0067, 0.0048, and 0.0067, respectively.

Sample	Path	nleg	N	R (Å)	σ^2 (Å2)	E0 (eV)
Zr-4L_1	Zr_1−O_1	2	4	2.09	0.0043	-2.382
	Zr_1−O_2	2	2	2.16	0.0043	-2.382
	Zr_1−O_4	2	2	2.18	0.0043	-2.382
	Zr_2−O_1	2	4	2.25	0.0046	-2.382
	Zr_2−O_3	2	4	2.31	0.0046	-2.382
	Zr_1−Zr_1	2	4	3.54	0.0040	-2.382
	Zr_2−Zr_1	2	4	3.55	0.0120	-2.382
Zr-4L_2	Zr_1−O_1	2	4	2.09	0.0043	-2.594
	Zr_1−O_2	2	2	2.16	0.0043	-2.594
	Zr_1−O_4	2	2	2.18	0.0043	-2.594
	Zr_2−O_1	2	4	2.24	0.0044	-2.594
	Zr_2−O_3	2	4	2.31	0.0044	-2.594
	Zr_1−Zr_1	2	4	3.55	0.0041	-2.594
	Zr_2−Zr_1	2	4	3.55	0.0150	-2.594
Zr-4L_3	Zr_1−O_1	2	4	2.09	0.0042	-2.331
	Zr_1−O_2	2	2	2.16	0.0042	-2.331
	Zr_1−O_4	2	2	2.18	0.0042	-2.331
	Zr_2−O_1	2	4	2.25	0.0040	-2.331
	Zr_2−O_3	2	4	2.31	0.0040	-2.331
	Zr_1−Zr_1	2	4	3.54	0.0118	-2.331
	Zr_2−Zr_1	2	4	3.54	0.0039	-2.331

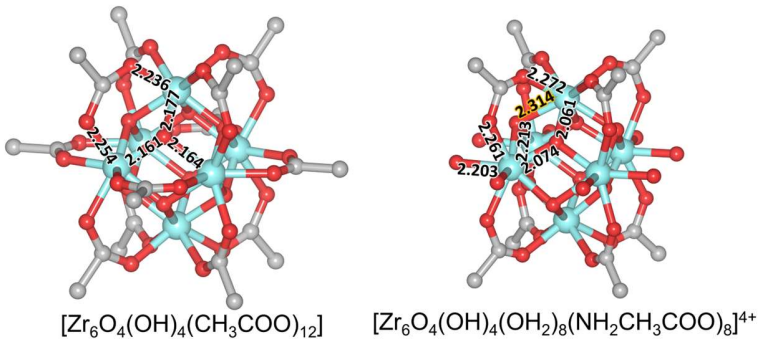

Fig. S48. Distance between Zr–O bonds of Zr_6 clusters with 12- and 8-bidentate bridging carboxylate coordination. The values are calculated from single crystal data of $Zr_6(O)_4(OH)_4(CH_3COO)_{12}\cdot 8.5H_2O$[8] and $[Zr_6(O)_4(OH)_4(H_2O)_8(Gly)_8]\cdot 12Cl\cdot 8H_2O$.[9]

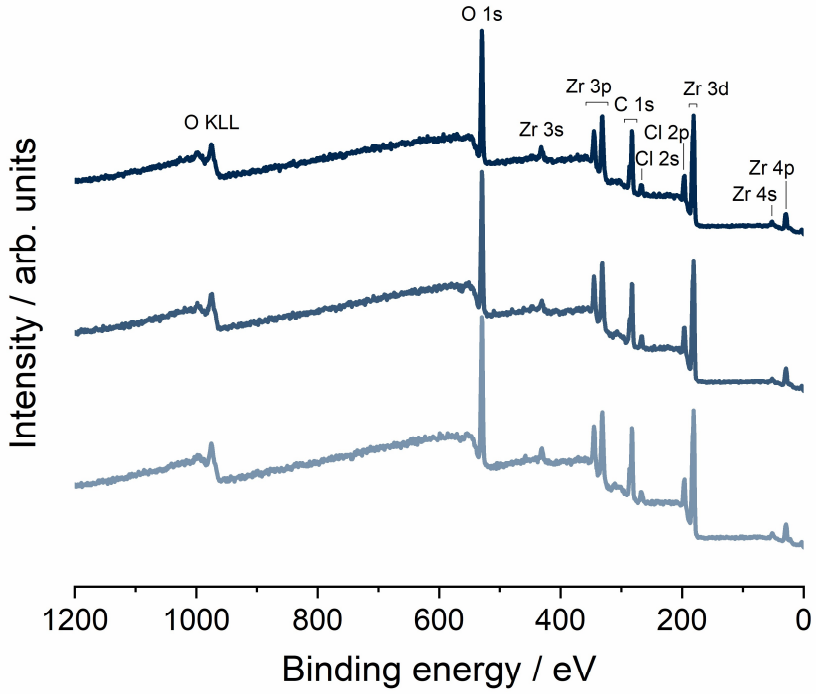

Fig. S49. XPS wide-scan spectra of ZrOAc cluster (3 repetitions).

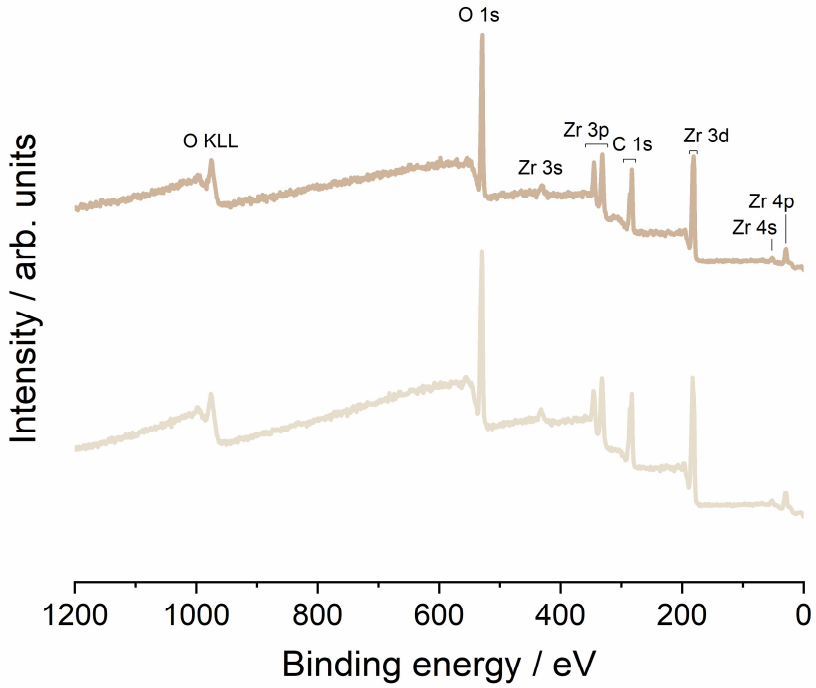

Fig. S50. XPS wide-scan spectra of Zr-4L_1 (2 repetitions).

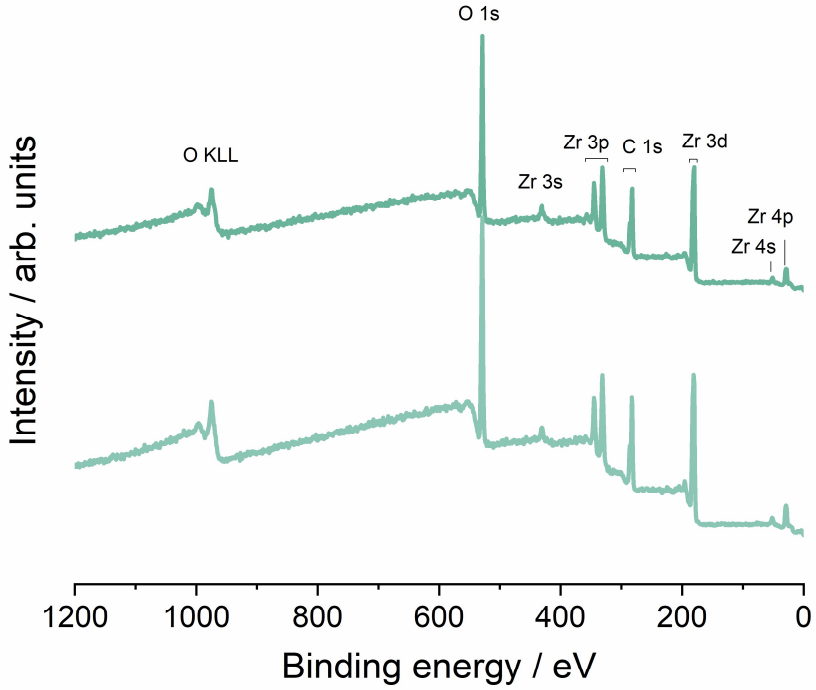

Fig. S51. XPS wide-scan spectra of Zr-4L_2 (2 repetitions).

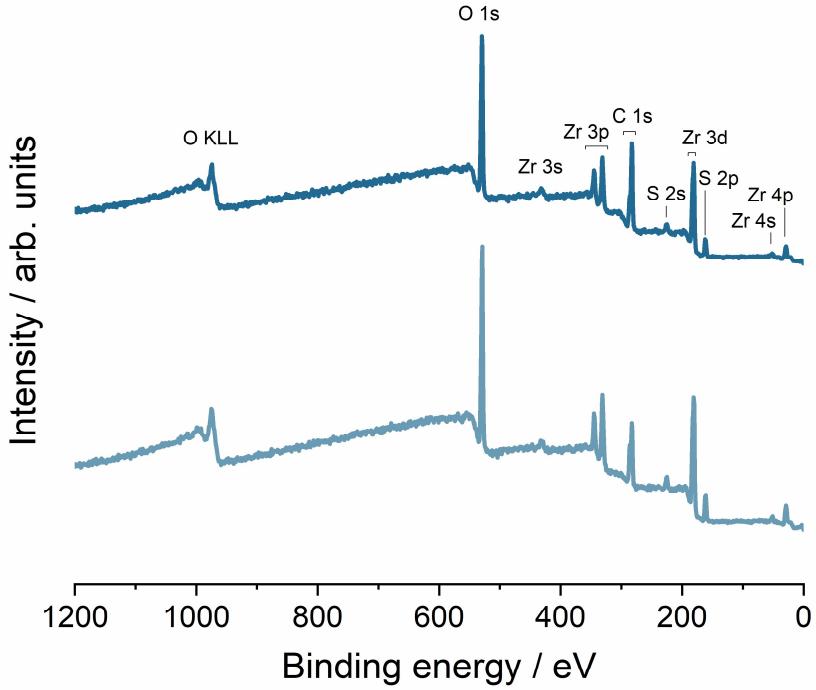

Fig. S52. XPS wide-scan spectra of Zr-4L$_3$ (2 repetitions).

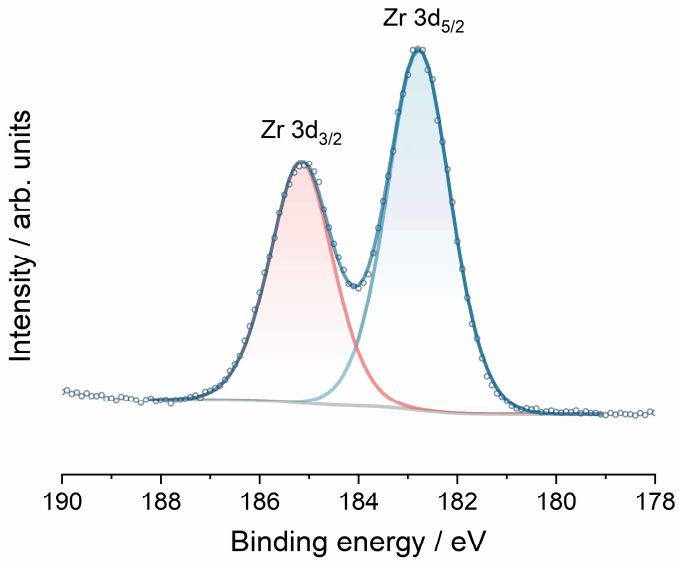

Fig. S53. Zr 3d XPS fitting of ZrOAc.

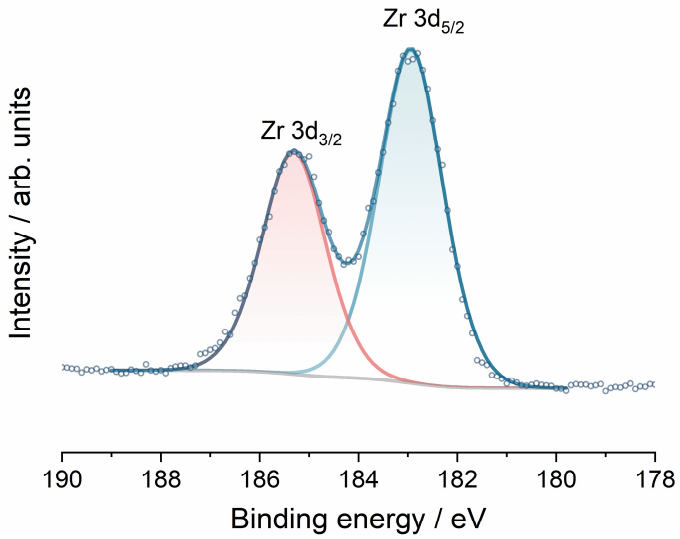

Fig. S54. Zr 3d XPS fitting of Zr-4L_1.

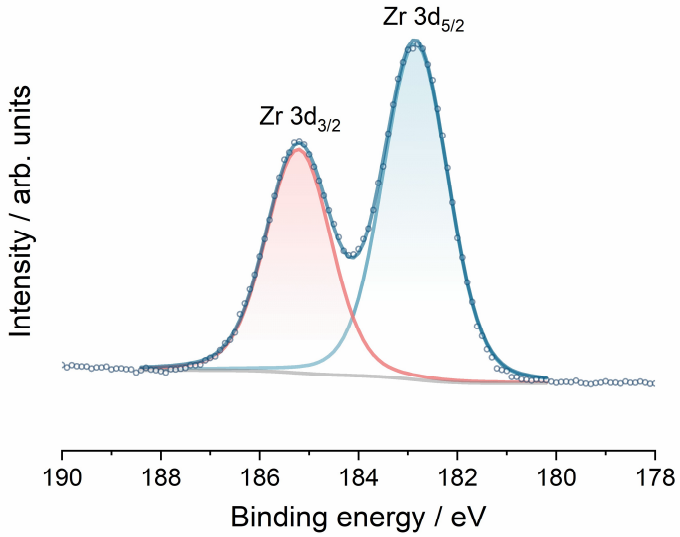

Fig. S55. Zr 3d XPS fitting of Zr-4L_2.

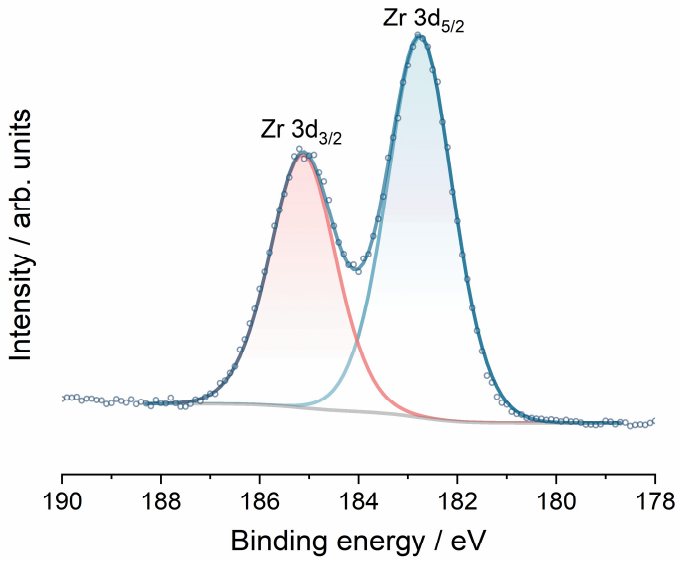

Fig. S56. Zr 3d XPS fitting of Zr-4L_3.

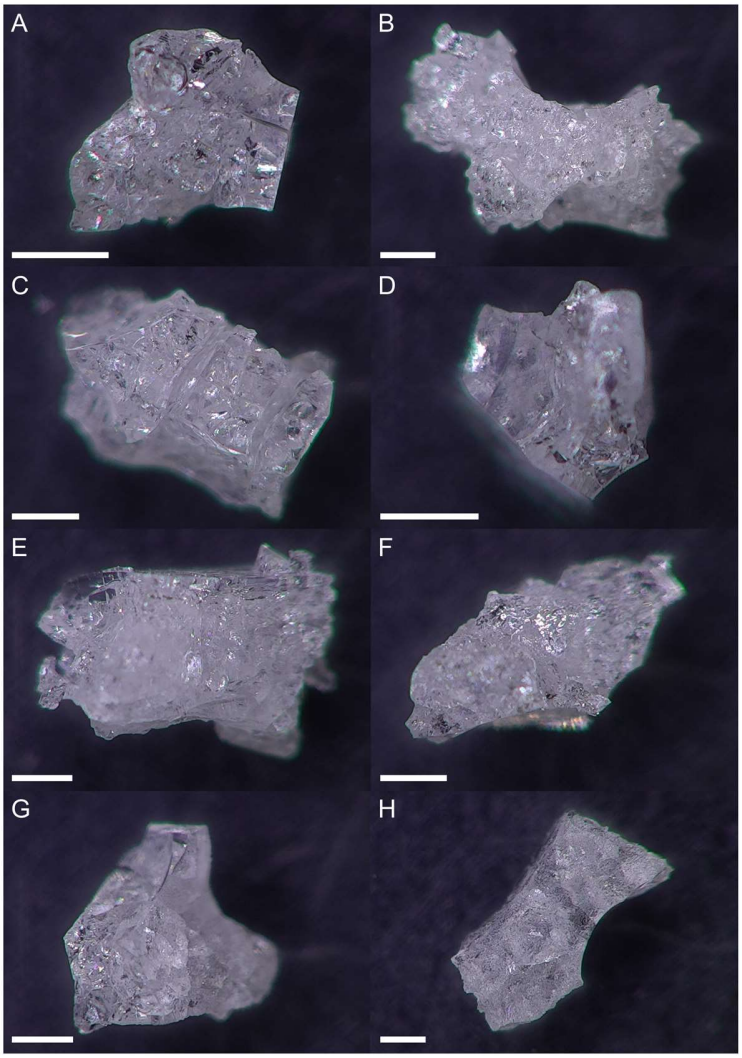

Fig. S57. Optical images of (A, B) Zr-2L_4, (C, D) Zr-4L_4, (E, F) Zr-8L_4, and (G, H) Zr-12L_4. The scale bars = 0.5 mm.

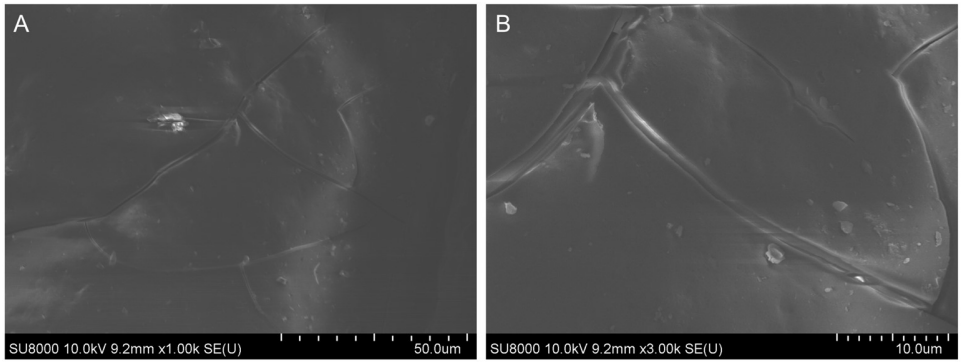

Fig. S58. SEM images of Zr-4L_4 at a magnification of (A) x1k and (B) x3k. Zr-4L_4 maintains a monolithic structure similar to Zr-4L_3, with a noticeably larger number of cracks.

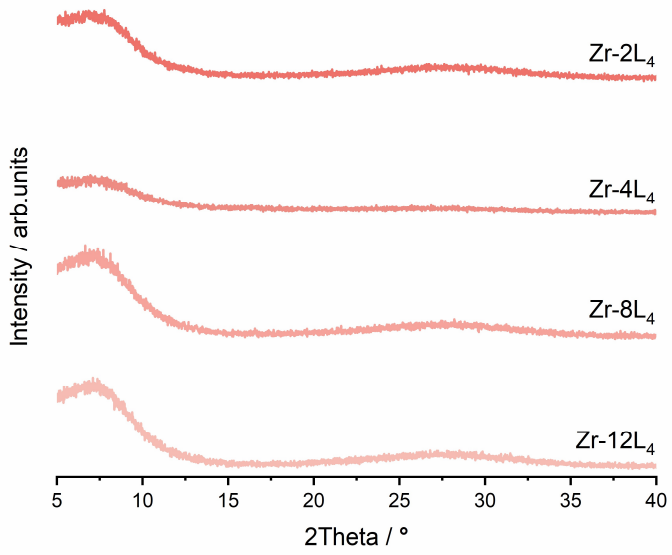

Fig. S59. PXRD (λ = 1.5406 Å) of Zr-2L$_4$, Zr-4L$_4$, Zr-8L$_4$, and Zr-12L$_4$.

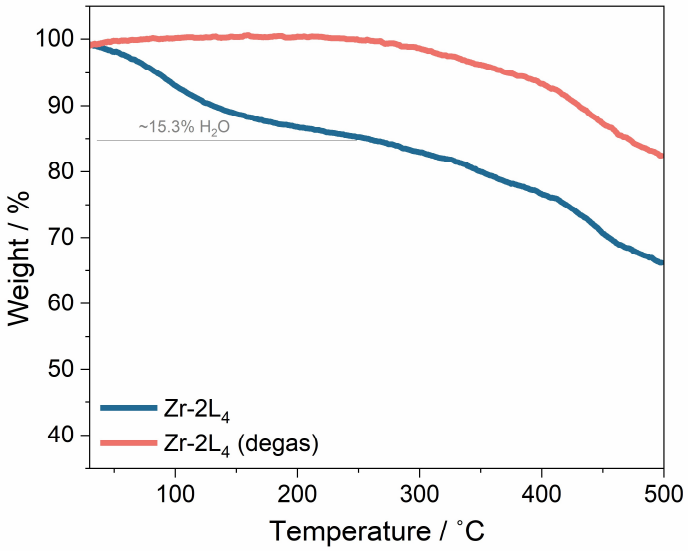

Fig. S60. TGA under of Zr-2L$_4$ (blue) and Zr-2L$_4$ after degas at 200 °C (red). The measurements were conducted under N_2 flow (50 mL min^{-1}) with heating rate of 10 °C min^{-1}.

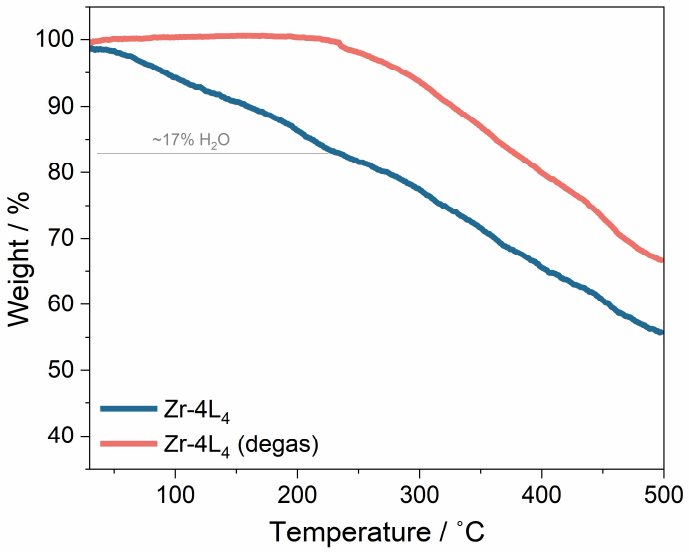

Fig. S61. TGA under of Zr-4L$_4$ (blue) and Zr-4L$_4$ after degas at 200 °C (red). The measurements were conducted under N_2 flow (50 mL min^{-1}) with heating rate of 10 °C min^{-1}.

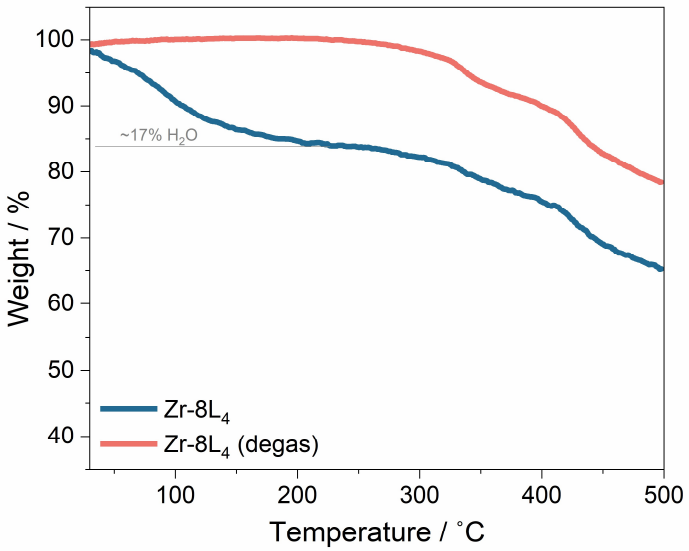

Fig. S62. TGA under of Zr-8L$_4$ (blue) and Zr-8L$_4$ after degas at 200 °C (red). The measurements were conducted under N_2 flow (50 mL min^{-1}) with heating rate of 10 °C min^{-1}.

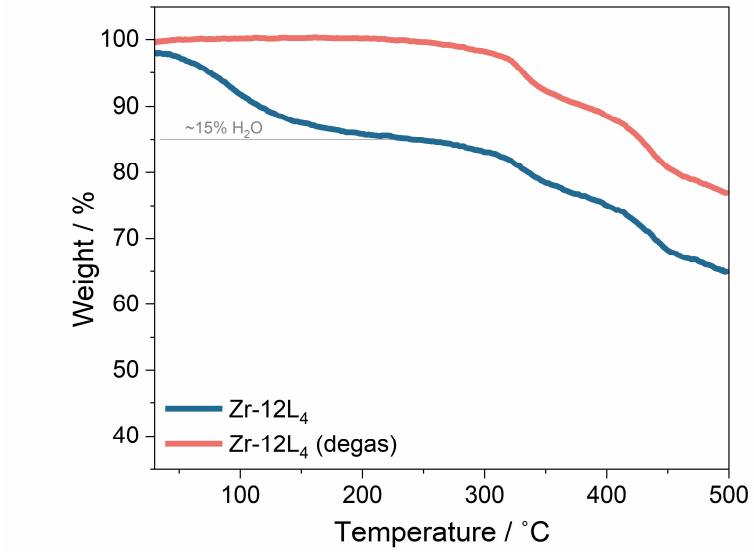

Fig. S63. TGA under of Zr-12L$_4$ (blue) and Zr-12L$_4$ after degas at 200 °C (red). The measurements were conducted under N_2 flow (50 mL min^{-1}) with heating rate of 10 °C min^{-1}.

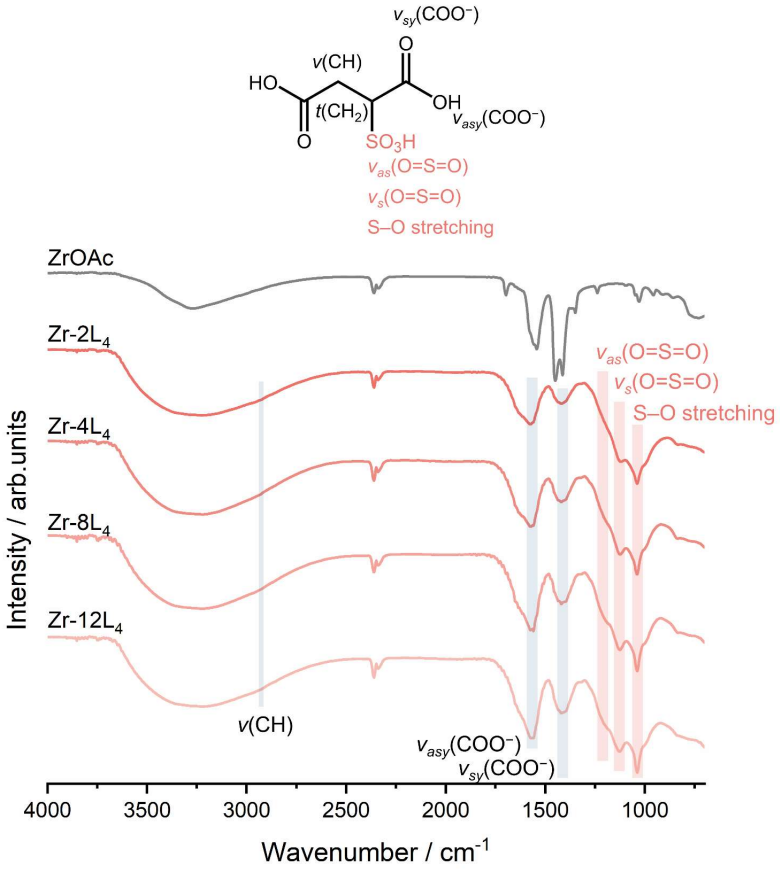

Fig. S64. FTIR of the ZrOAc cluster, Zr-2L$_4$, Zr-4L$_4$, Zr-8L$_4$, and Zr-12L$_4$.

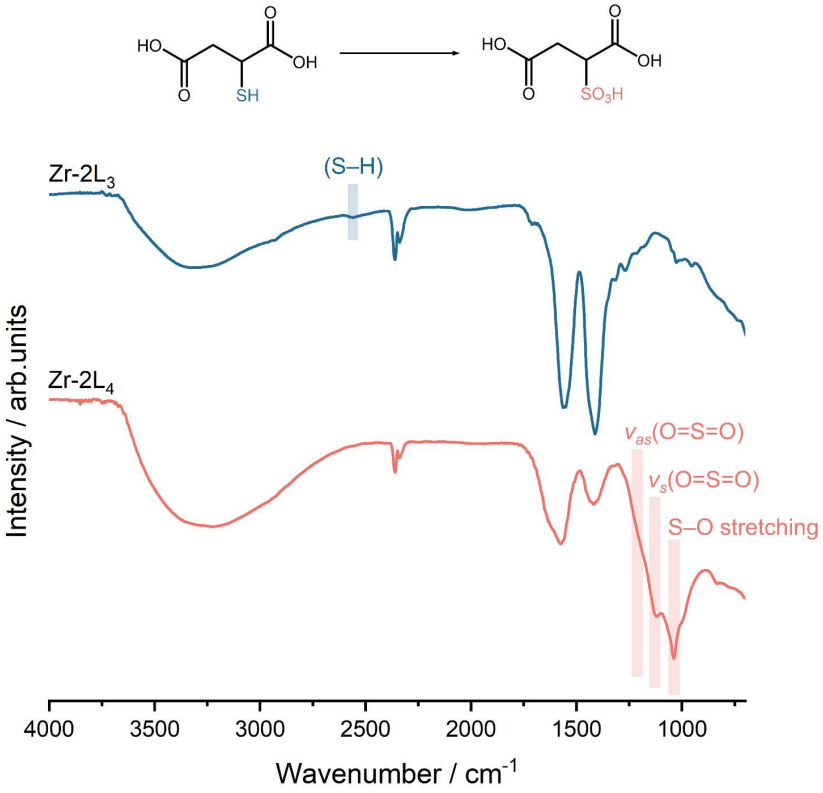

Fig. S65. FTIR of the Zr-2L$_3$ and Zr-2L$_4$.

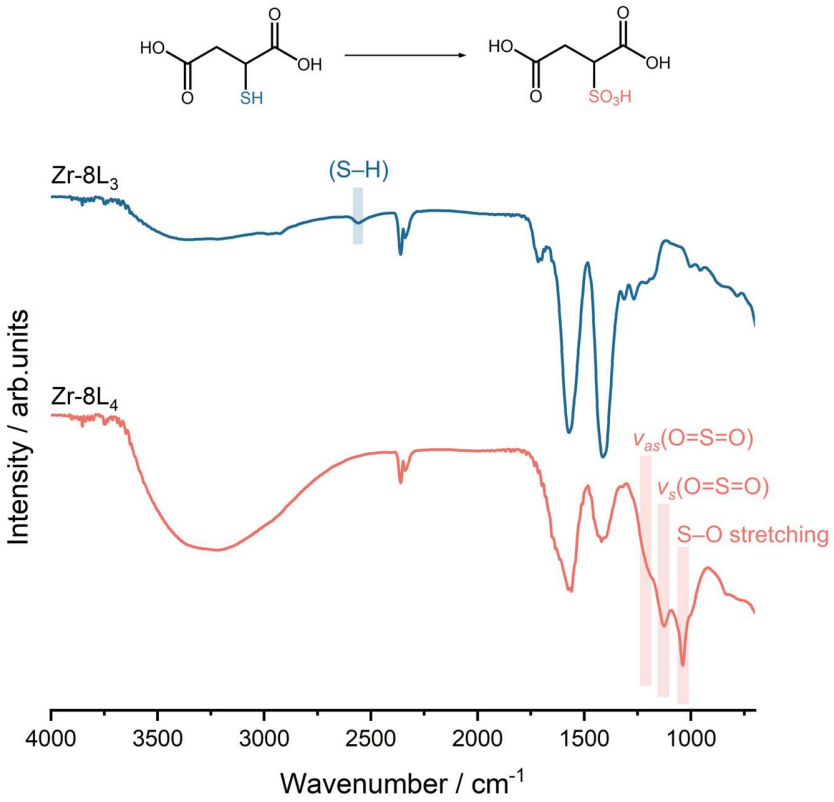

Fig. S66. FTIR of the Zr-8L_3 and Zr-8L_4.

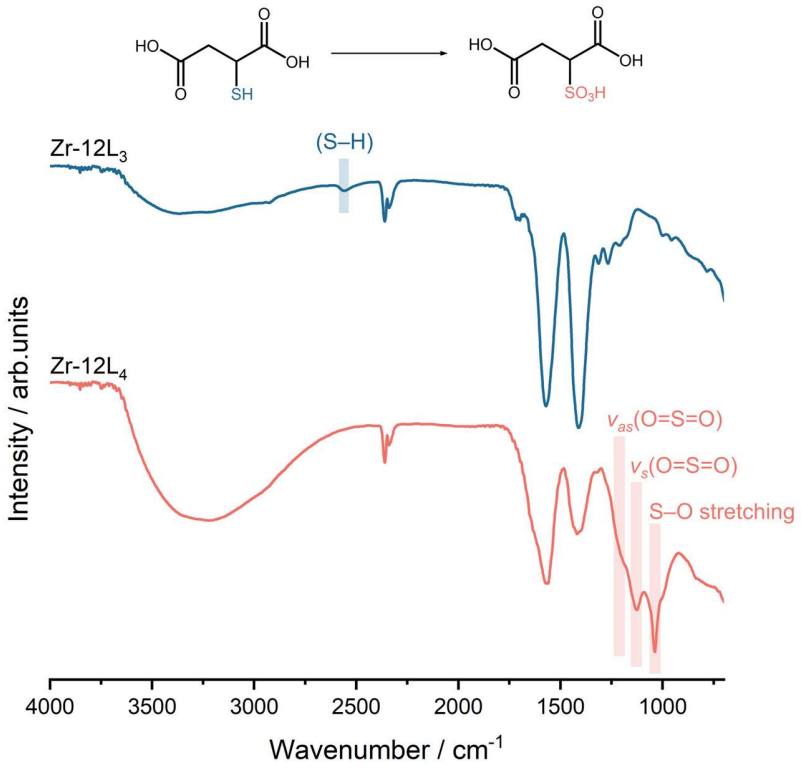

Fig. S67. FTIR of the Zr-12L_3 and Zr-12L_4.

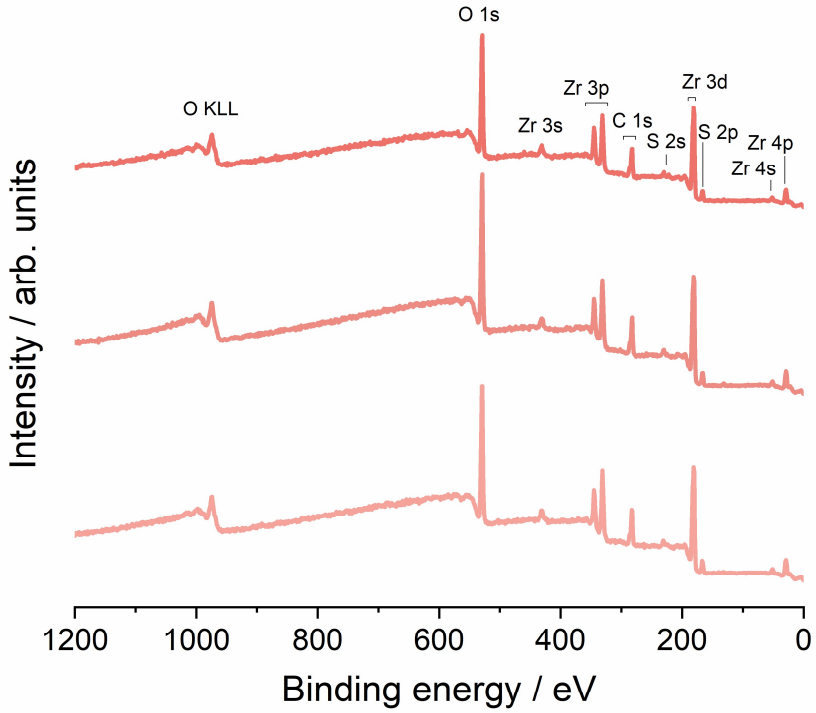

Fig. S68. XPS wide-scan spectra of Zr-4L$_4$ (3 repetitions).

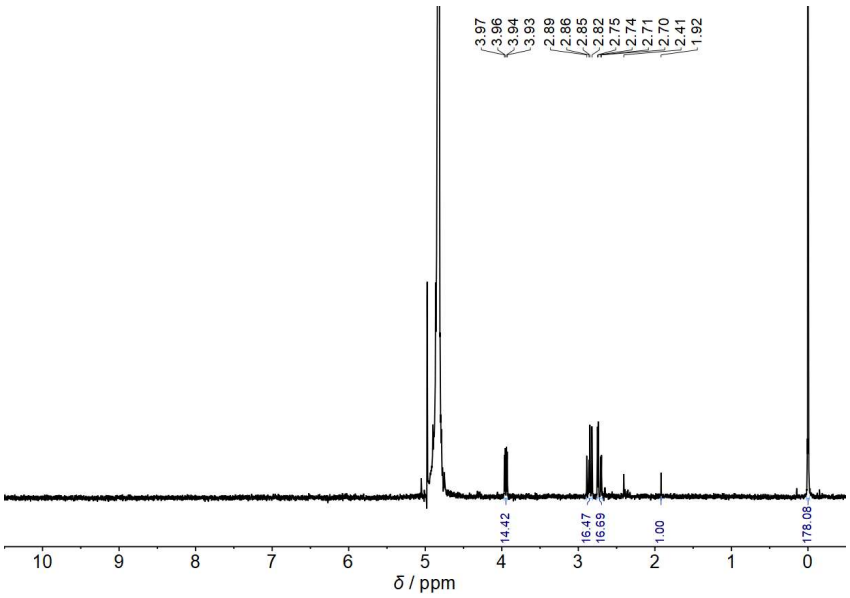

Fig. S69. ^{1}H NMR (400 MHz, D_2O) spectrum of Zr-4L$_4$.

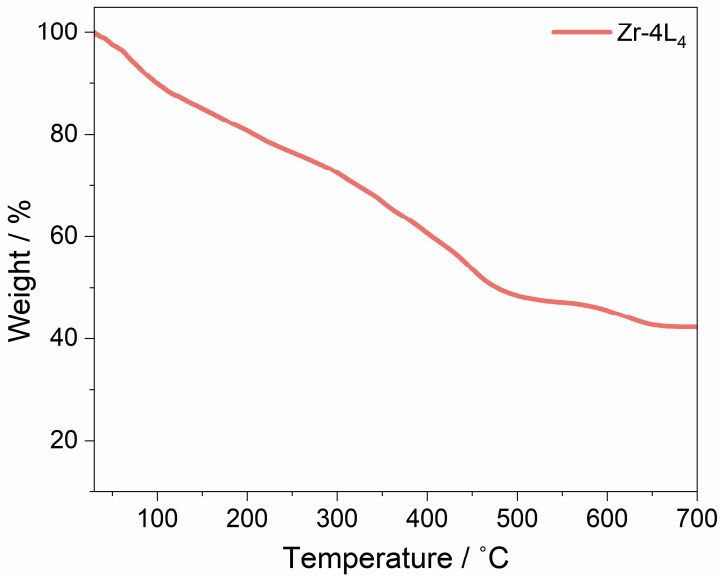

Fig. S70. TGA of Zr-4L$_4$ from 30 to 700 °C. The measurements were conducted under air flow (100 mL min^{-1}) with a heating rate of 10 °C min^{-1}. The bridging ligand contents are determined from weight loss between 285 °C and 700 °C.

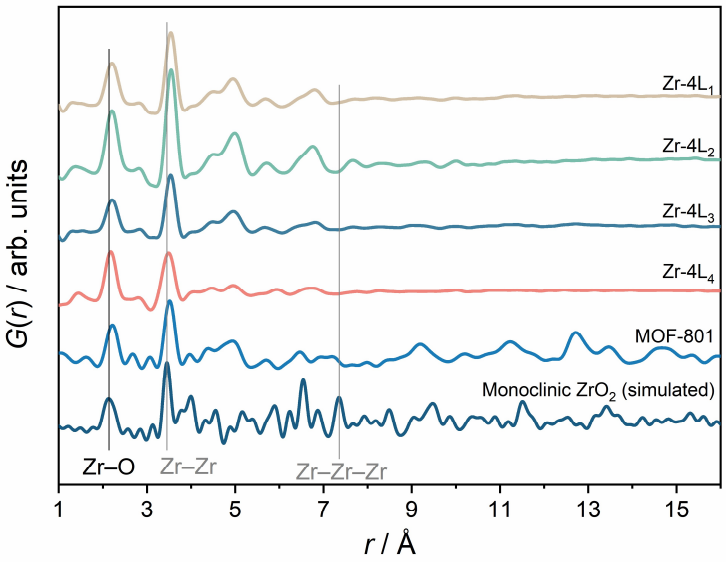

Fig. S71. Pair distribution function (PDF) results of Zr-4L$_1$, Zr-4L$_2$, Zr-4L$_3$, Zr-4L$_4$, MOF-801, and simulated PDF of monoclinic ZrO_2. The simulated PDF was generated via PDFgui 2.0.3 software[7] with the crystal structure from ref 10. The absence of amorphous ZrO_2 or $Zr(OH)_4$ byproduct was confirmed by comparing the Zr–O and Zr–Zr pair distances in the aMOFs with the simulated PDF data for monoclinic ZrO_2. We found that the Zr–O (2.13 Å) and Zr–Zr (3.45 Å) pair distances in ZnO_2 are considerably smaller than those in any aMOFs. Additionally, none of the aMOF samples exhibited peak features around 7.35 Å, which corresponds to the in-plane Zr–O–Zr–O–Zr correlation expected for ZrO_2. Note that monoclinic ZrO_2 and amorphous $Zr(OH)_4$ share similar low-*r* PDF features[11].

Table S2. Zr K-edge EXAFS data fitting result of Zr-4L$_4$. The R-factor is 0.0048.

Sample	Path	nleg	N	R (Å)	σ^2 (Å2)	E0 (eV)
	Zr_1–O_6	2	2	1.77	0.0414	-4.106
	Zr_1–O_1	2	4	2.14	0.0026	-4.106
	Zr_1–O_2	2	2	2.78	0.0122	-4.106
	Zr_1–S_2	2	2	3.28	0.0041	-4.106
	Zr_1–Zr_4	2	3	3.47	0.0112	-4.106
	Zr_2–O_{16}	2	2	2.06	0.0049	-4.106
	Zr_2–O_{19}	2	6	2.24	0.0049	-4.106
Zr-4L$_4$	Zr_3–O_{16}	2	1	2.04	0.0143	-4.106
	Zr_3–O_6	2	1	1.77	0.0143	-4.106
	Zr_3–O_{11}	2	4	2.21	0.0143	-4.106
	Zr_3–O_2	2	2	2.23	0.0143	-4.106
	Zr_3–S_2	2	2	3.57	0.0041	-4.106
	Zr_3–Zr_1	2	3	3.50	0.0112	-4.106
	Zr_4–O_6	2	2	2.03	0.0312	-4.106
	Zr_4–O_7	2	6	2.68	0.0312	-4.106

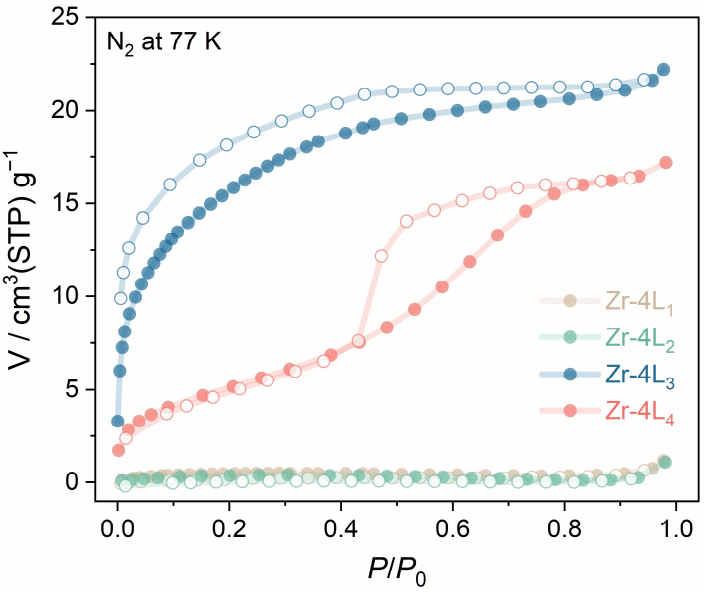

Fig. S72. Gas sorption analysis of Zr-4L$_1$, Zr-4L$_2$, Zr-4L$_3$, and Zr-4L$_4$ via N_2 sorption isotherms collected at 77 K.

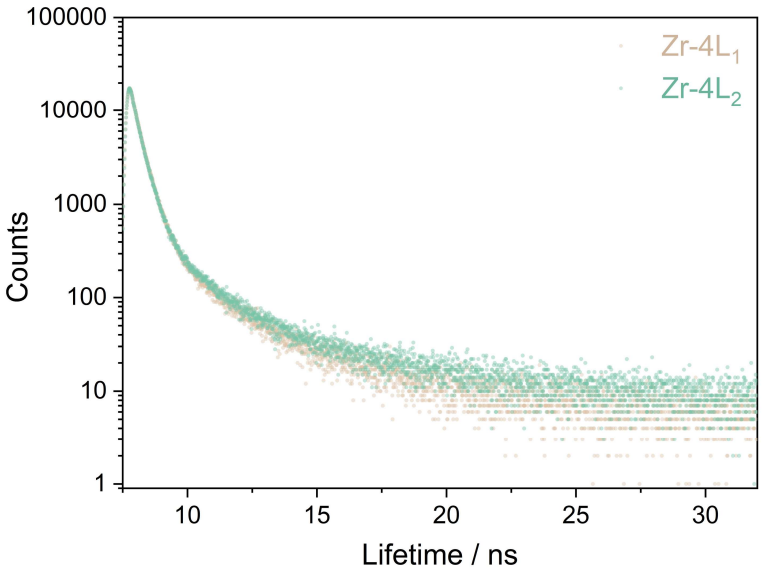

Fig. S73. Positron annihilation lifetimes of Zr-4L$_1$ and Zr-4L$_2$.

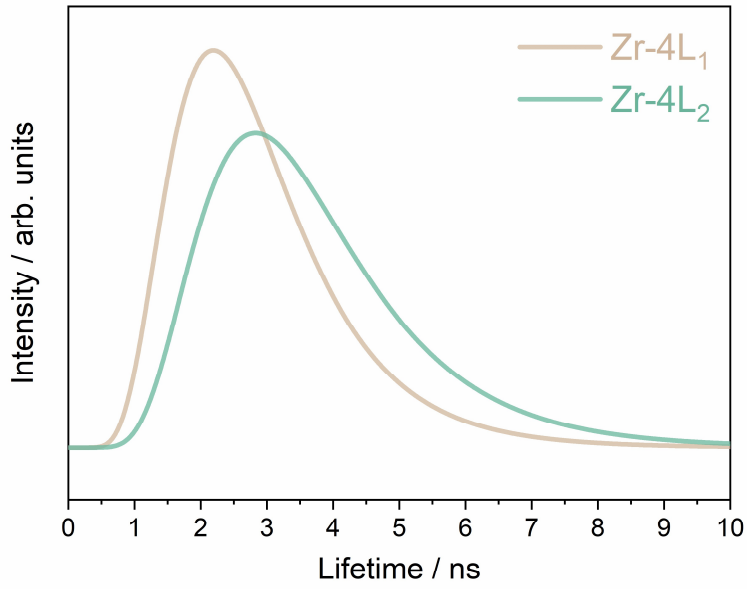

Fig. S74. Lifetime distribution of Zr-4L$_1$ and Zr-4L$_2$ from positron annihilation lifetime spectroscopy (PALS).

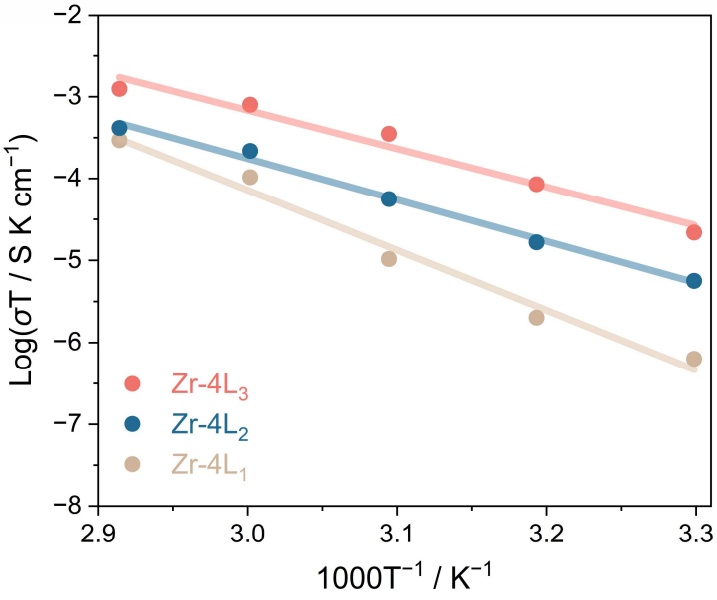

Fig. S75. Arrhenius plots of the H^+ conductivity under a relative humidity of 95%.

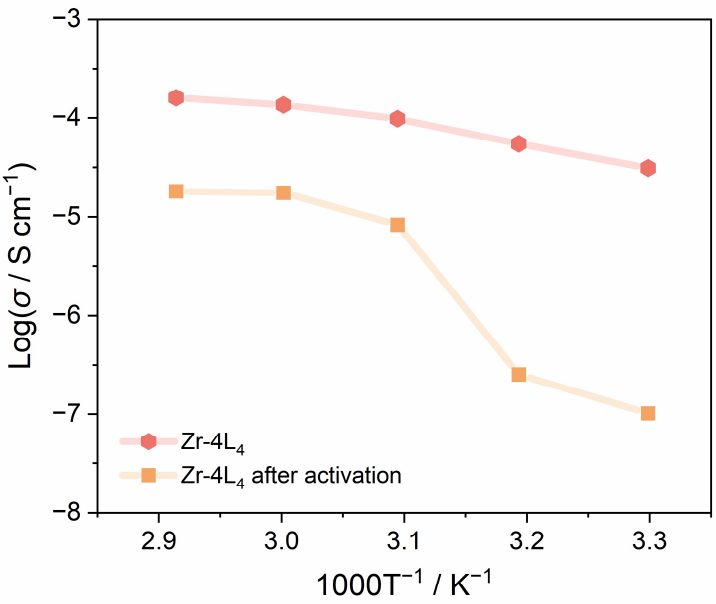

Fig. S76. Variable-temperature H^+ conductivity measurements at 95% RH of Zr-4L4 and Zr-4L4 after activation. Activation was performed by heating Zr-4L4 at 130 °C for 12 h under vacuum. Following activation, the sample was maintained at 30 °C 95% RH for 12 h before the conductivity measurement at 95% RH. The results indicated that Zr-4L4 irreversibly lost its interstitial water guest molecules after activation, resulting in a decrease in overall H^+ conductivity.

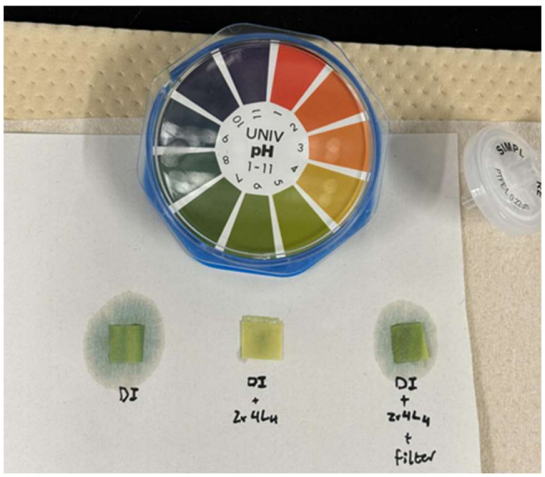

Fig. S77. Acidity test to confirm the absence of residual free sulfuric acid. The test included (left) DI water, (middle) suspension of Zr-4L4 in DI water, and (left) filtrate of Zr-4L4 soaked in DI water. 15 mg of Zr-4L4 was soaked in 1 ml DI water for 10 minutes. The mixture was then filtered using a PTFE 0.22 μm syringe filter to remove any particles, and the pH of the filtrate was measured with pH test paper (ADVANTEC, UNIV).

References

1. S. Dai, C. Simms, I. Dovgaliuk, G. Patriarche, A. Tissot, T. N. Parac-Vogt and C. Serre, Monodispersed MOF-808 Nanocrystals Synthesized via a Scalable Room-Temperature Approach for Efficient Heterogeneous Peptide Bond Hydrolysis, *Chem. Mater.*, 2021, **33**, 7057–7066.
2. T. E. Faber and J. M. Ziman, A theory of the electrical properties of liquid metals, *Philos. Mag.*, 1965, **11**, 153–173.
3. E. Lorch, Neutron diffraction by germania, silica and radiation-damaged silica glasses, *J. Phys. C: Solid State Phys.*, 1969, **2**, 229–237.
4. S. Kohara, M. Itou, K. Suzuya, Y. Inamura, Y. Sakurai, Y. Ohishi and M. Takata, Structural studies of disordered materials using high-energy x-ray diffraction from ambient to extreme conditions, *J. Phys. Condens. Matter.*, 2007, **19**, 506101.
5. H. Furukawa, F. Gándara, Y.-B. Zhang, J. Jiang, W. L. Queen, M. R. Hudson and O. M. Yaghi, Water Adsorption in Porous Metal–Organic Frameworks and Related Materials, *J. Am. Chem. Soc.*, 2014, **136**, 4369–4381.
6. S. Øien, D. Wragg, H. Reinsch, S. Svelle, S. Bordiga, C. Lamberti and K. P. Lillerud, Detailed Structure Analysis of Atomic Positions and Defects in Zirconium Metal–Organic Frameworks, *Cryst. Growth Des.*, 2014, **14**, 5370–5372.
7. C. L. Farrow, P. Juhas, J. W. Liu, D. Bryndin, E. S. Božin, J. Bloch, T. Proffen and S. J. L. Billinge, PDFfit2 and PDFgui: computer programs for studying nanostructure in crystals, *J. Phys.: Condens. Matter*, 2007, **19**, 335219.
8. C. Hennig, S. Weiss, W. Kraus, J. Kretzschmar and A. C. Scheinost, Solution Species and Crystal Structure of Zr(IV) Acetate, *Inorg. Chem.*, 2017, **56**, 2473–2480.
9. I. Pappas, M. Fitzgerald, X.-Y. Huang, J. Li and L. Pan, Thermally Resolved in Situ Dynamic Light Scattering Studies of Zirconium(IV) Complex Formation, *Cryst. Growth Des.*, 2009, **9**, 5213–5219.
10. D. K. Smith and W. Newkirk, The crystal structure of baddeleyite (monoclinic ZrO2) and its relation to the polymorphism of ZrO_2, *Acta Cryst.*, 1965, **18**, 983–991.
11. G. King, J. R. Soliz and W. O. Gordon, Local structure of $Zr(OH)_4$ and the effect of calcination temperature from X-ray pair distribution function analysis, *Inorg. Chem.*, 2018, **57**, 2797–2803.